Journal of Hydrology 588 (2020) 125043

Contents lists available at ScienceDirect

Journal of Hydrology

journal homepage: www.elsevier.com/locate/jhydrol

Research papers

Evaluation and validation of a high spatial resolution satellite soil moisture product over the Continental United States

Bin Fang[a,*], Venkataraman Lakshmi[a], Rajat Bindlish[b], Thomas J. Jackson[c], Pang-Wei Liu[b]

[a] Department of Engineering Systems and Environment, University of Virginia, Charlottesville, VA 22904, United States
[b] Hydrological Sciences Branch, NASA Goddard Space Flight Center, Greenbelt, MD 20771, United States
[c] United States Department of Agriculture (Retired), Beltsville, MD 20705, United States

ARTICLE INFO

This manuscript was handled by Corrado Corradini, Editor-in-Chief

Keywords:
SMAP
Soil moisture downscaling
In situ validation

ABSTRACT

The soil moisture (SM) data retrieved from the Soil Moisture Active and Passive (SMAP) satellite are available at a 9 km grid spacing since April 2015. This product can provide valuable information for research and applications in hydrology and other related fields. However, the resolution may be too coarse for applications at catchment or field scale. In this study, an established downscaling methodology, which had a major modification regarding its application on the SMAP 33 km domain, was implemented to develop a 1 km soil moisture product based on the SMAP 9 km data. The algorithm proposed here is based on the thermal inertia principle and developed by modeling the relationship between surface temperature difference and SM for different Normalized Difference Vegetation Index (NDVI) classes. The model functions were established and tuned using data from the NASA's Land Information System (LIS) North America Land Data Assimilation System (NLDAS) and remotely sensed VISible/InfRared (VIS/IR) reflectance data from Long Term Data Record (LTDR) AVHRR (Advanced Very High Resolution Radiometer) for the growing season months of April-September 1981–2018. These were then implemented using the MODIS (Moderate Resolution Imaging Spectroradiometer) data over the Continental United States (CONUS) domain. Validation activities were carried out using *in situ* measurements distributed through the International Soil Moisture Network (ISMN). The validation results computed using the 1 km SM data showed that the R^2, unbiased RMSE (root mean square error) and bias were improved relative to the 9 km SMAP product by 0.045, 0.018 m^3/m^3 and 0.001 m^3/m^3, respectively. The 1 km SM also exhibited a strong time-series autocorrelation. Further accuracy assessment analyses indicated that precipitation might contribute to the uncertainties in both the 9 km SMAP and 1 km downscaled SMAP SM products.

1. Introduction

Soil moisture (SM) observations provide important information for studying the exchange of water and energy between the land and the atmosphere and serve as a key input variable in numerical models for weather forecasting, ecology, and agriculture applications as well as the prediction of hydrological extremes such as floods and droughts. As compared to point scale SM from ground-based sensors, satellite observations (in particular microwave-based remote sensing) provide routine and almost continuous global coverage (Lakshmi et al., 1997; Lakshmi, 2004). During the past decades, a number of active and passive microwave satellites have been launched that are capable of measuring surface moisture at a global scale. These include Advanced Microwave Scanning Radiometer for the Earth Observing System (AMSR-E) (Njoku et al., 2003; Jackson et al., 2010; Sridhar et al., 2013), Advanced Microwave Scanning Radiometer 2 (AMSR2) (Imaoka et al., 2010; Oki et al., 2010, Bindlish et al, 2018), Advanced SCATterometer (ASCAT) (Wagner et al., 2013; Kim et al., 2018), Aquarius (Bindlish et al., 2015), Soil Moisture and Ocean Salinity (SMOS) (Kerr et al., 2001, Jackson et al., 2012) and Soil Moisture Active/Passive (SMAP) (McNairn et al., 2014, Chan et al., 2016; Colliander et al., 2017a; Chan et al., 2018; Kim and Lakshmi, 2018). The L-band microwave radiometer observations are preferred because they provide more reliable surface SM information (accuracy and contributing depth) (Schmugge et al., 1986; Jackson 1993; Schmugge and Jackson, 1994; Njoku and Entekhabi, 1996; Lakshmi and Susskind, 2000; Lakshmi, 2013; Lakshmi, 2014). Although Radio Frequency Interference (RFI) effect was a concern at L-band, the SMAP mission has addressed RFI through avoidance and filtering approaches. (Spencer et al., 2013; Piepmeier et al., 2013; Colliander et al., 2017a).

* Corresponding author.
E-mail address: bf3fh@virginia.edu (B. Fang).

https://doi.org/10.1016/j.jhydrol.2020.125043
Received 29 April 2020; Accepted 2 May 2020
Available online 08 May 2020

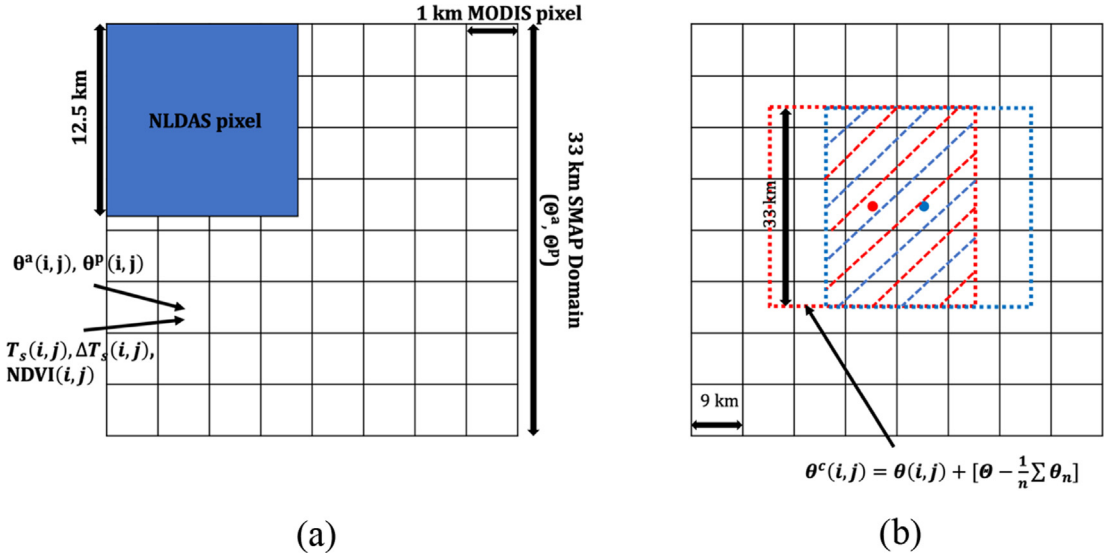

Fig. 1. Conceptual diagram of (a) fitting and implementing the $\theta - \Delta T_s$ relationship from NLDAS model grid size (12.5 km) to MODIS pixel size (1 km); (b) performing downscaling of the 9 km SMAP SM using SM which is calculated from $\theta - \Delta T_s$ model at 33 km domain. The red and blue boxes denote the two adjacent 33 km domains of the 9 km apart SMAP SM points. (For interpretation of the references to colour in this figure legend, the reader is referred to the web version of this article.)

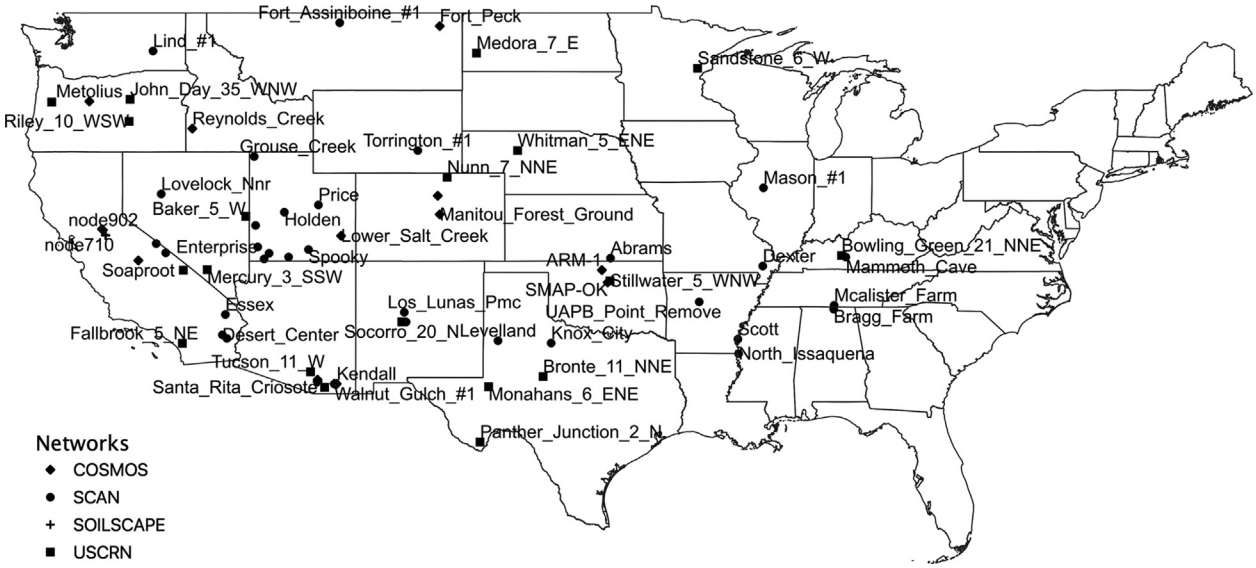

Fig. 2. Locations of the ISMN ground stations used to validate the downscaled 1 km SM product. The selected stations are part of the COSMOS, SCAN, SoilSCAPE and USCRN networks covering different CONUS states.

The spatial resolution of the currently available passive microwave SM products is on the order of tens of kilometers, which is determined by the antenna aperture (Le Vine et al., 1994). Such spatial resolution does not satisfy the demands of many hydrological or agricultural studies that require the characterization of SM variability at finer scales. Recent research examined the use of downscaling algorithms as a solution to the spatial resolution problem (Merlin et al., 2015; Peng et al., 2017; Sabaghy et al., 2018). The available downscaling algorithms can be classified as (1) using data from satellite observations. For example, some of the proposed methods have downscaled coarse resolution passive microwave SM retrievals which rely on the use of higher resolution radar observations (Bindlish and Barros, 2002; Bolten et al., 2003; Narayan et al., 2004; Narayan et al, 2006; Narayan and Lakshmi, 2008; Fang et al., 2019; Zhan et al., 2017), or satellite VIS/IR (Visible/Infrared) observations (Piles et al., 2011; Piles et al., 2014; Fang et al., 2013; Colliander et al., 2017b), (2) using information from the other related land surface variables such as vegetation and soil properties (Fang and Lakshmi, 2014a; Kim et al., 2017; Merlin et al., 2010, 2013; Mishra et al., 2018; Peng et al., 2015, 2016; Tagesson et al., 2018), or (3) statistical-based or model-based (land surface model, LSM) approaches using derived geophysical variables at high spatial resolution (Sánchez-Ruiz et al., 2014; Zhao et al., 2018).

In this investigation, we implemented a modified SM downscaling algorithm based on thermal inertia principle and used satellite VIS/IR observations to downscale the enhanced 9 km SMAP data. We validated the 1 km downscaled and 9 km SMAP SM observations and discussed their performances over the CONUS domain.

A detailed description of the original downscaling algorithm applied here can be found in Fang et al. (2013). The algorithm originally exploited the previously well-studied NDVI modulated relationship between SM and surface temperature (Gillies et al., 1997; Carlson, 2007; Mallick et al., 2009; Minacapilli et al., 2009; Lakshmi et al., 2001; Lakshmi et al., 2011). In this investigation, a major modification was performed to downscale the enhanced 9 km SMAP SM over the 33 km

Table 1
Descriptions of the ISMN data, including SM network, number of stations, period of records, land cover types and main soil types.

SM Network	Number of Stations	Period of Records	Land Cover Types	Main Soil Types
COSMOS	14	2015–2018	Grassland, shrubland, forest	Sand, clay
SCAN	32	2015–2018	Rainfed cropland, grassland, shrubland, urban area, forest	Sand, clay
SoilSCAPE	35	2015–2016	Grassland, shrubland	Sand
USCRN	19	2015–2018	Grassland, shrubland, forest	Sand, clay

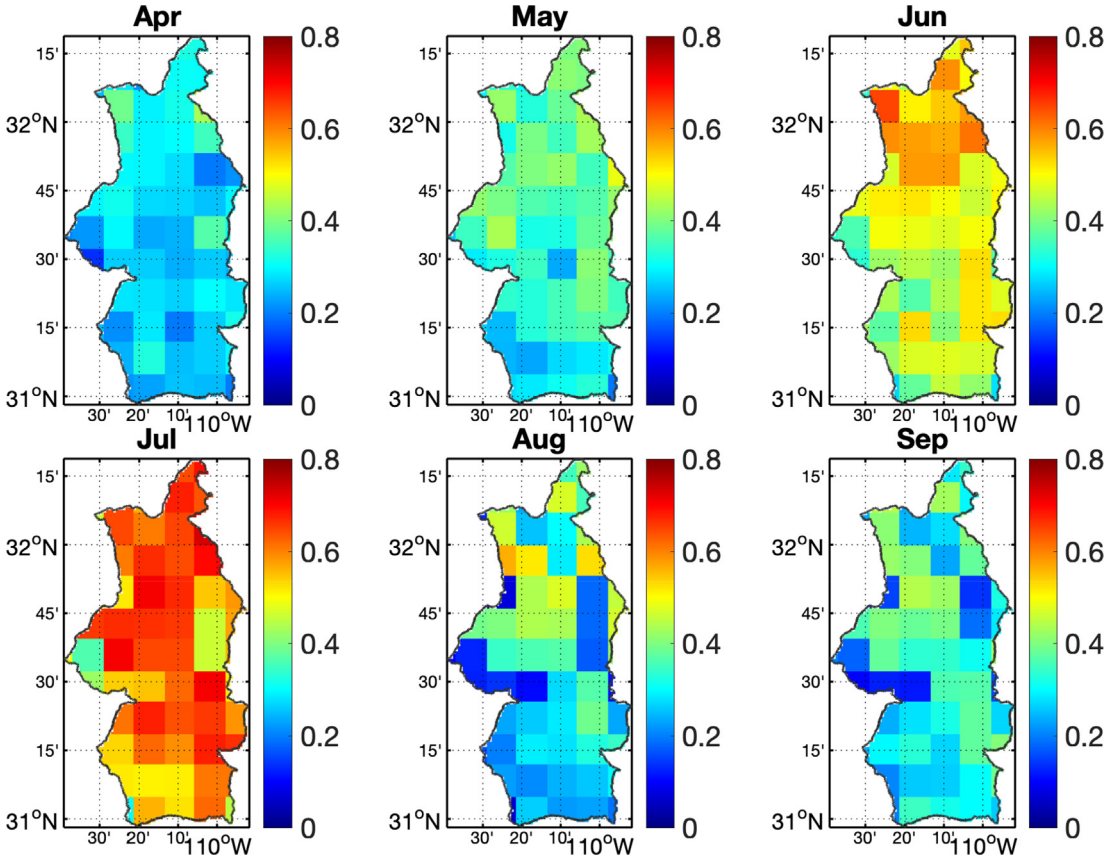

Fig. 3. R^2 from the NLDAS derived $\theta - \Delta T_s$ linear regression fit between the months of April and September at the SMAP descending overpass (6:00 a.m.) over the San Pedro Watershed. The grid values represent the average R^2 from all NDVI classes.

domain, which is the contributing domain of SMAP radiometer observations. It utilizes the high spatial resolution satellite surface temperature and VIS/IR-based vegetation index from MODIS to produce a wide coverage and routinely available SM retrievals (Fang and Lakshmi, 2014b; Fang et al., 2018a; Fang et al., 2018b; Senanayake et al., 2019; Dandridge et al., 2020).

2. Brief description of the downscaling methodology

The original downscaling algorithm is based on the thermal inertia theory that wetter objects tend to have a greater volumetric heat capacity and lower temperature change, and vice versa for dry objects. The assumption made is that the rate of change in surface soil moisture is negatively correlated to the rate of change in surface temperature (Matsushima et al., 2012). This is especially true during the summer months when the evapotranspiration rate is the dominant factor. Therefore, in the application of the algorithm, it is assumed that the maximum diurnal surface temperature difference can be estimated by the difference of surface temperature between the two overpass times of Aqua MODIS 1:30 p.m. (time of maximum surface temperature) and 1:30 a.m. (time of minimum surface temperature) (Fang et al., 2013), and this would correspond to the SMAP SM overpasses, i.e. 6:00 a.m. or 6:00 p.m. The relationship between the NLDAS Noah model derived surface skin temperature change ΔT_s and SM θ between 1981 and 2018 can be modeled using a linear regression fit. The LTDR NDVI data were used to classify the corresponding NLDAS $\theta - \Delta T_s$ relationship by grouping them at an interval of 0.1 over the 0 – 1 NDVI range. The relationship was then developed separately for each class and applied on 1 km MODIS LST grids which were included within the corresponding NLDAS grid's boundaries, to calculate the 1 km SM. We made an assumption that the spatial variability of the $\theta - \Delta T_s$ relationship within one NLDAS grid could be ignored.

The 1 km SM calculated from the $\theta - \Delta T_s$ model needs to be adjusted by the difference between SMAP 9 km SM and the average of all 1 km $\theta - \Delta T_s$ model output grids located in the 33 km contributing domain, which is the native spatial area to the 9 km SMAP radiometer T_B grid (Chan et al., 2018). This modification can effectively reduce the sharp edge effect which is most likely caused by the errors of NLDAS and MODIS data. This is the major improvement of the original downscaling algorithm developed by Fang et al. (2013).

The conceptual diagram of the model building, implementation, and downscaling is given in Fig. 1.

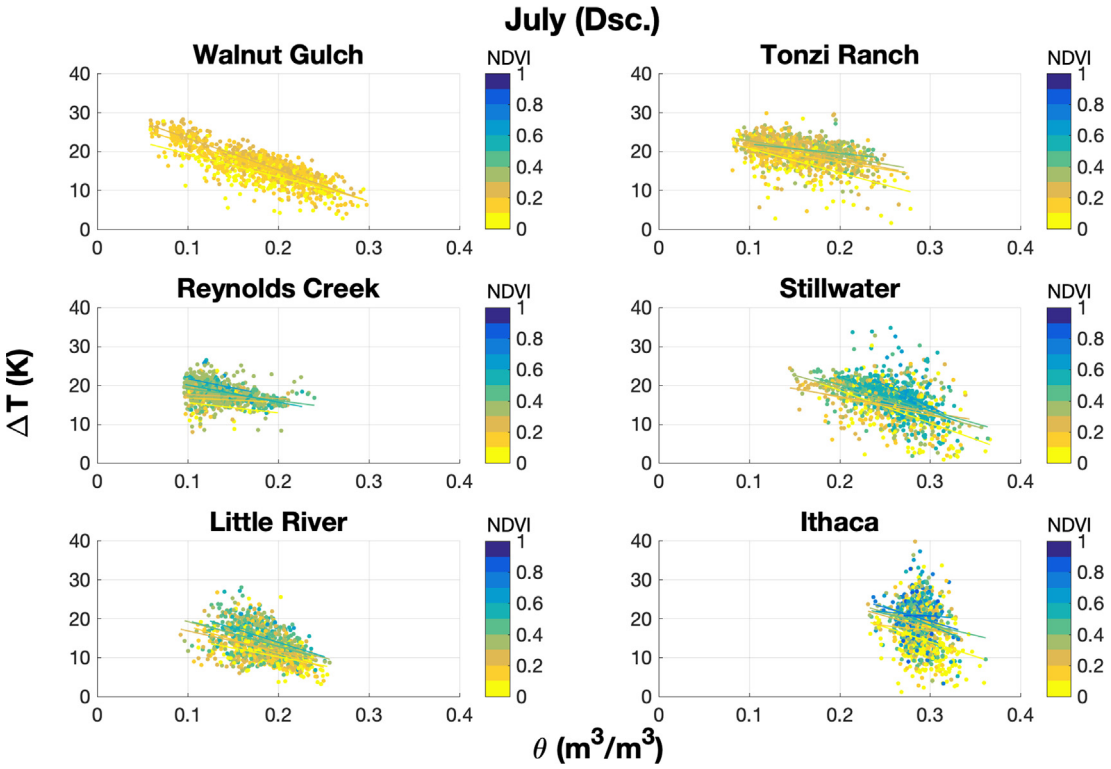

Fig. 4. Scatter plots of the $\theta - \Delta T_s$ agreement for the month of July (1981–2018) computed per NDVI class for the descending overpass SMAP θ.

Table 2
R^2 from the linear regression fit of the $\theta - \Delta T_s$ relationship of different NDVI classes from descending overpass in July between 1981 and 2018 at the six selected NLDAS grids in CONUS: San Pedro Basin, Tonzi Ranch, Reynolds Creek, Stillwater, Little River and Ithaca. Each site represents different vegetation cover and SM conditions.

NDVI	San Pedro Basin	Reynolds Creek	Tonzi Ranch	Stillwater	Little River	Ithaca
0–0.1	0.516	0.251	0.417	0.28	0.243	0.126
0.1–0.2	0.707	0.197	0.408	0.13	0.286	0.074
0.2–0.3	0.782	0.266	0.222	0.142	0.165	0.127
0.3–0.4	–	0.234	0.213	0.284	0.183	0.068
0.4–0.5	–	–	–	0.305	0.189	0.118
0.5–0.6	–	–	–	0.243	0.215	0.014
0.6–0.7	–	–	–	0.171	–	0.064
0.7–0.8	–	–	–	–	–	0.011
0.8–0.9	–	–	–	–	–	0.195

3. Study area and data description

3.1. Study area

The SM downscaling algorithm was used to derive a downscaled 1 km soil moisture product using the available SMAP 9 km daily SM product between 2015 and 2018 over the CONUS domain. A major reason for limiting the spatial domain to CONUS was determined by the need of long-term estimates of surface skin temperature change ΔT_s and SM θ. One way to address this need at a global scale is to use readily available model-based products. The regression model was applied by utilizing the NLDAS model output data, which provides spatial coverage limited to the CONUS area at 12.5 km model grid spacing.

3.2. Data

3.2.1. NLDAS data

NLDAS provides forcing data and LSM data at hourly time step and 12.5 km model grid spacing. It spans from January 1979 to the present. NLDAS data integrates LSM datasets and ground observations. In this study, we used the NLDAS NOAA (National Oceanic and Atmospheric Administration) Noah LSM Level 4 variables: surface skin temperature (unit: K) and SM (unit: m^3/m^3) at 0–10 cm (http://ldas.gsfc.nasa.gov/nldas/) to build the $\theta - \Delta T_s$ model. The NLDAS Noah model was developed from the NCEP (National Centers for Environmental Prediction) mesoscale Eta model. There have been numerous publications on validation of the NLDAS data, such as Ek et al. (2003), Schaake et al., 2004, Mitchell et al. (2004) and Xia et al. (2013), Fang et al. (2016).

3.2.2. LTDR NDVI data

The LTDR is a project launched by NASA for publishing global surface climate data record and currently the LTDR Version 5 NDVI is derived from NOAA satellites N07 ~ N19 (AVH13C1) AVHRR (1981 – present) and Terra/Aqua MODIS (2000 - present) (Pedelty et al., 2007). The daily NDVI product is originally projected at 0.05° spatial resolution Climate Modeling Grid (CMG) and is available at https://ltdr.nascom.nasa.gov/. The previous study showed a strong overall correlation of 0.87 between AVHRR and MODIS NDVI data, which suggested that the MODIS NDVI data could be used to supplement the existing AVHRR historical data (Bédard et al., 2006). In this study, we only used the LTDR AVHRR data and upscaled it to 12.5 km resolution to match with NLDAS grids for the $\theta - \Delta T_s$ model building.

3.2.3. MODIS products

MODIS is onboard two NASA satellites Terra and Aqua. MODIS provides daily observations of land surface variables, including radiation, temperature and vegetation at a global scale. It has a total of 36 visible/infrared bands, which range between 250 m and 1 km spatial resolution (Tucker, 1979; Wan and Li, 1997). In this study, the 1 km daily Aqua MODIS LST (MYD11A1) and the biweekly NDVI products (MYD13A2) were acquired from Land Processes Distributed Active Archive Center (LP DAAC) at https://lpdaac.usgs.gov/.

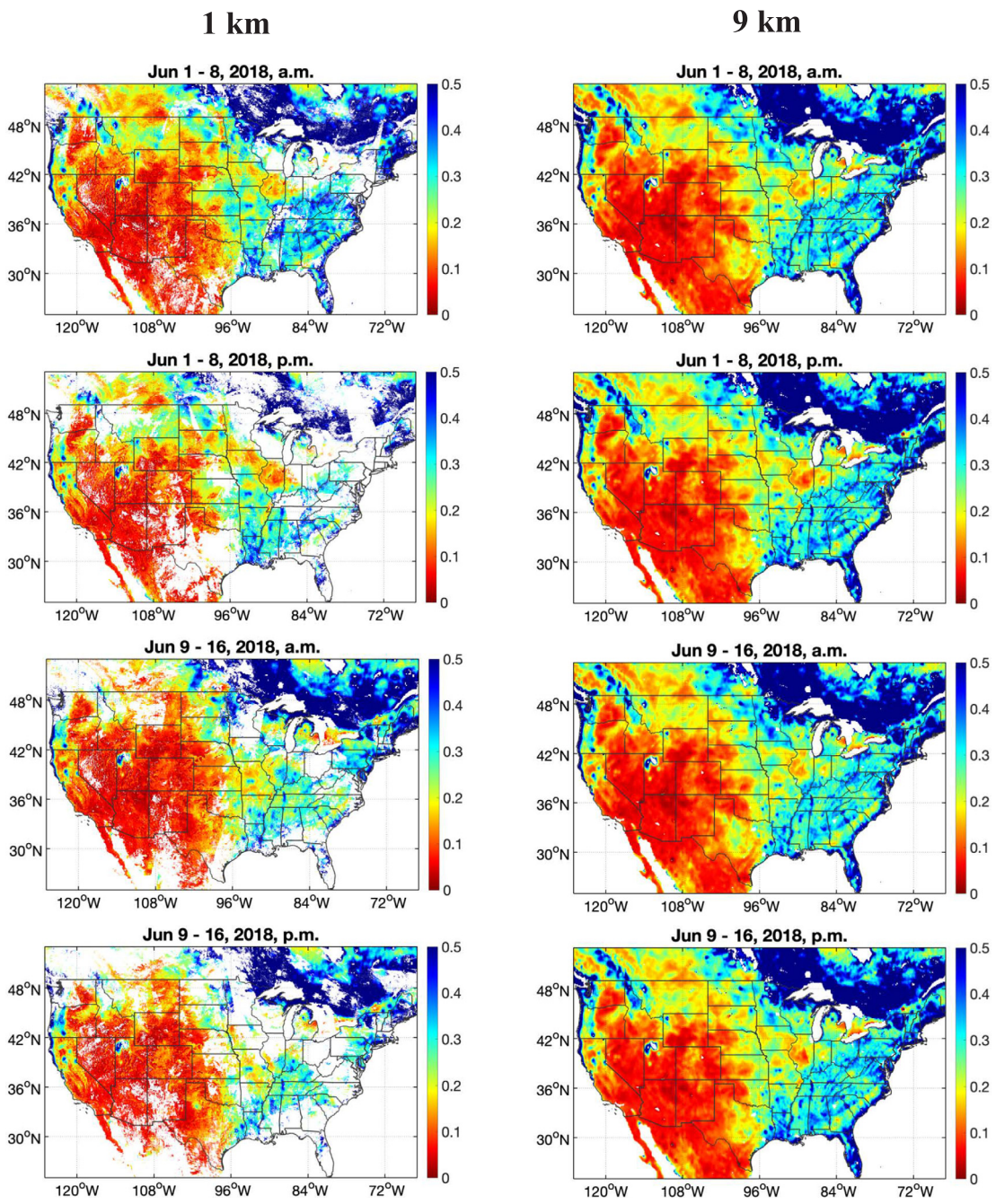

Fig. 5. 8-day composites of the 1 km downscaled and the original 9 km SMAP L2 half-orbit enhanced radiometer SM retrievals. Maps display the results from the ascending and the descending overpasses during the 1st half of June 2018.

3.2.4. SMAP data

The SMAP mission was launched in January 2015, and it has an L-band mission (radiometer centered at 1.41 GHz) that operates in a near-polar sun-synchronous orbit. It has a revisit time of 2–3 days and observes the Earth at 6 a.m/6 p.m. The SM estimates represent the top 0–5 cm of soil layer with a threshold of vegetation water content ≤ 5 kg/m^2 (Chan et al., 2016). In this study, the enhanced Level-2 half orbit 9 km SM product (SPL2SMP_E) was acquired from NSIDC (National Snow and Ice Data Center) at https://nsidc.org/data/SPL2SMP_E for downscaling. The SMAP SM retrievals are solely derived from the L-band radiometer T_B data using the Single Channel Algorithm (Jackson, 1993) at the native spatial resolution of 33 to 40 km. The retrievals are enhanced to 9 km EASE (Equal Area Scalable Earth) grid using the approach developed by Chan et al. (2018), which is based on interpolating antenna temperature data in the original SMAP Level 1B T_B data, by using Backus-Gilbert optimal interpolation technique.

3.2.5. GPM (global precipitation measurement) data

The GPM satellite mission is designed to provide new standard rainfall and snowfall observations at a global scale every 3 h. This satellite has Dual-Frequency DPR (Precipitation Radar) and GMI (GPM Microwave Imager) mounted and extends the measurement range of the TRMM (Tropical Rainfall Measuring Mission) (Hou et al., 2014; Huffman et al., 2015). The IMERG (Integrated Multi-satellitE Retrievals for GPM) precipitation data were downloaded from https://pmm.nasa.gov/data-access/downloads/gpm and were used as reference data, to study the SM spatial and temporal variability of the downscaled SM as

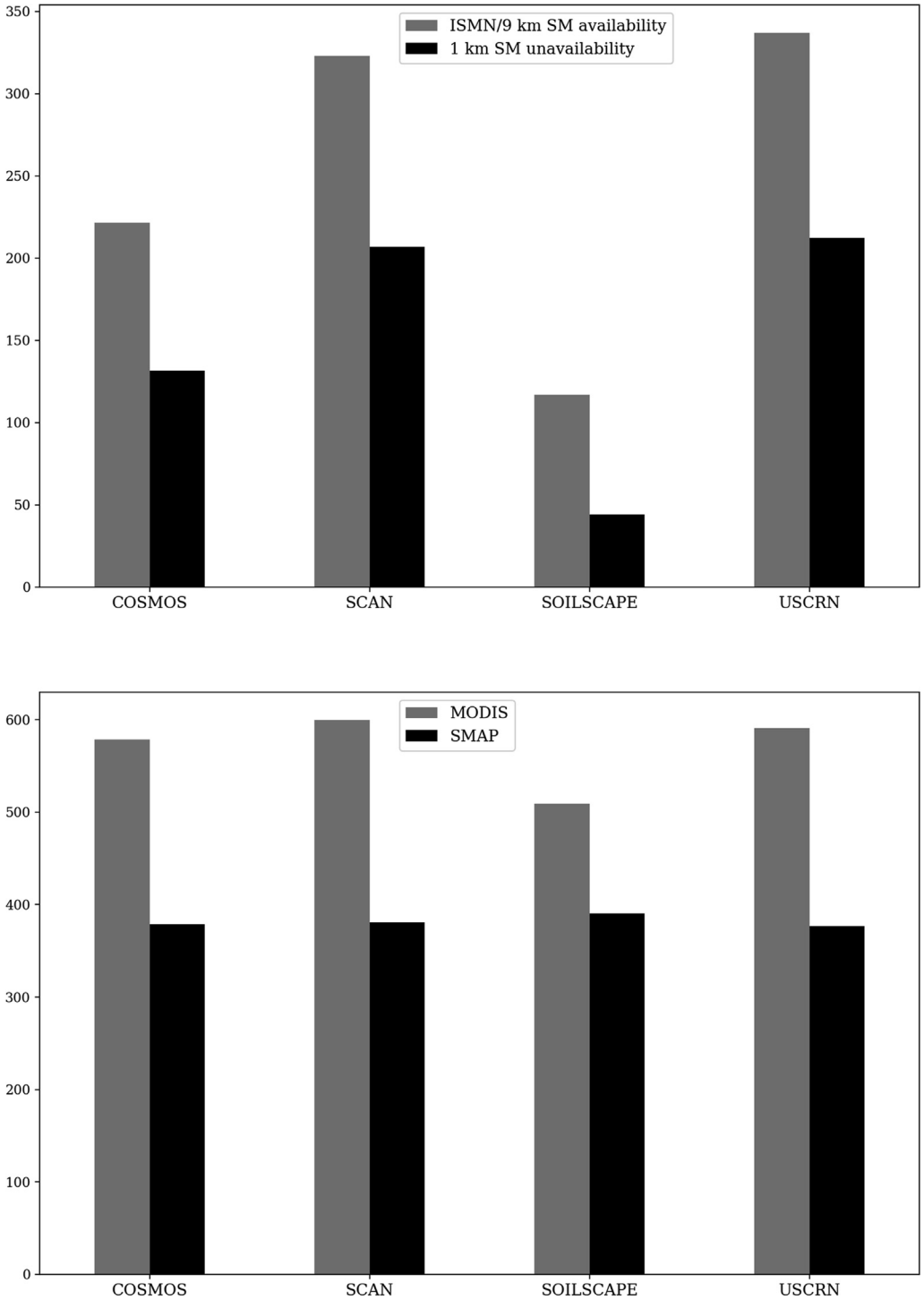

Fig. 6. For the 4 SM networks: (a) the average number of days between 2015 and 2018 which have both ISMN and 9 km SMAP SM data versus the average number of days which have no 1 km downscaled SMAP SM data; (b) the average number of days between 2015 and 2018 from MODIS LST/9 km SMAP data which account for the missing days of the 1 km downscaled SMAP SM data.

well as the influence of precipitation on the performance of the downscaling algorithm.

3.2.6. ISMN data

The ISMN hosts *in situ* SM measurements collected starting 1952 to present from a total of 35 international SM networks, which include more than 1400 stations. The purpose of ISMN is to validate, calibrate and improve the accuracy of remote sensing SM retrieval algorithms and LSM SM outputs as well as to provide other variable measurements, including soil temperature and precipitation for the better interpretation of soil moisture (Dorigo et al., 2011, 2013; Gruber et al., 2013). The ISMN data from the various SM networks were downloaded from https://ismn.geo.tuwien.ac.at/. Discussions and evaluations of the accuracy and uncertainties between different ISMN soil networks can be found in the research by Han et al. (2014), Rosolem et al. (2013), Zreda et al. (2012), Coopersmith et al. (2016), Bell et al. (2013a,b) and Diamond et al. (2013).

The downscaled SMAP 1 km SM estimates were evaluated using *in*

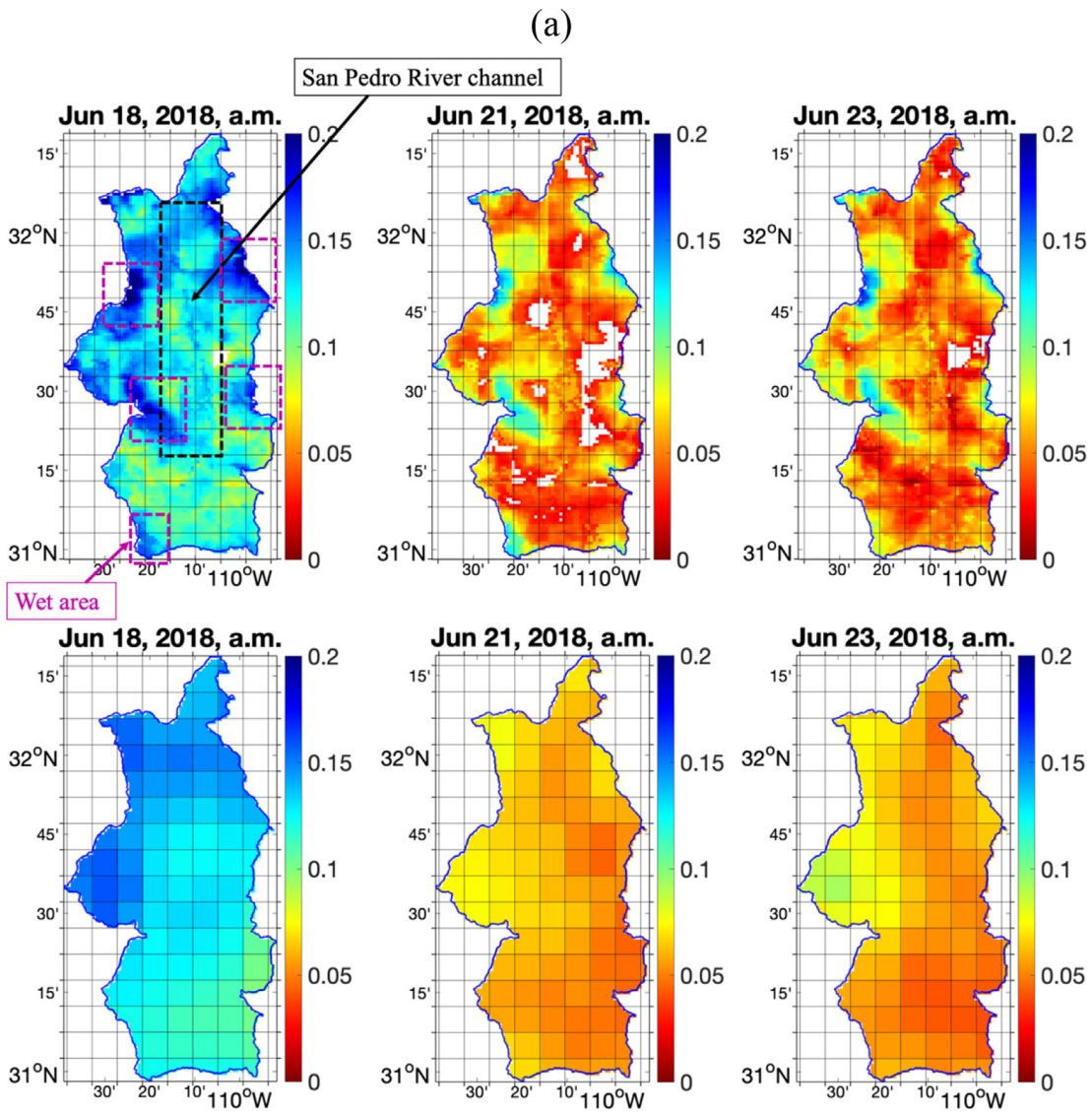

Fig. 7. (a) 1 km downscaled SM comparing with 9 km SMAP SM of descending overpass between June 18 – 23, 2018 at San Pedro Watershed, AZ. The 9 km SMAP grids are outlined. The black dotted line box outlines the channel of San Pedro River and the pink dotted line boxes outline the wet areas which are only captured by 1 km SM maps, (b) Difference map between the 1 km and 9 km SMAP SM, and the accumulated GPM precipitation (unit: mm) between June 16 – 17, which was the only rainfall occurred during this time period. (For interpretation of the references to colour in this figure legend, the reader is referred to the web version of this article.)

situ SM measurements from 100 ISMN stations in CONUS. As the Fig. 2 shows, the validation data include the stations from 4 SM networks for validating SMAP SM retrieval algorithms. The ISMN SM networks include: COSMOS (COsmic-ray Soil Moisture Observation System), SoilSCAPE (Soil Moisture Sensing Controller And oPtimal Estimator), USCRN (U.S. Climate Reference Network) and SCAN (Soil Climate Analysis Network). Table 1 shows the brief descriptions of the 4 SM networks. These stations cover different types of climate zones, soil properties, land cover types, and vegetation types, which allow us to thoroughly examine the performance of the downscaling algorithm over the CONUS domain. In addition, the San Pedro watershed was used for mapping 1 km / 9 km SMAP SM and showing the spatial and temporal SM variabilities.

4. Results and analyses

4.1. θ-ΔT model evaluation

The Eqs. (1) – (5) of the statistical variables (R^2, unbiased RMSE, bias, spatial standard deviation and average) are shown below. They were used for evaluating and validating the 1 km/9 km SMAP SM estimates as well as the model performance (Willmott, 1982).

$$R^2 = 1 - \frac{\sum (\theta_i - \widehat{\theta_i})^2}{\sum \left(\theta_i - \bar{\theta}\right)^2} \quad (1)$$

$$b = \frac{\sum_{i=1}^{n} (\theta_i - \widehat{\theta_i})}{n} \quad (2)$$

$$ubRMSE = \sqrt{\frac{\sum_{i=1}^{n} (\theta_i - (\widehat{\theta_i} - b))^2}{n}} \quad (3)$$

$$\sigma = \sqrt{\frac{\sum_{i=1}^{n} \left(\bar{\theta} - \widehat{\theta_i}\right)^2}{n}} \quad (4)$$

(b)

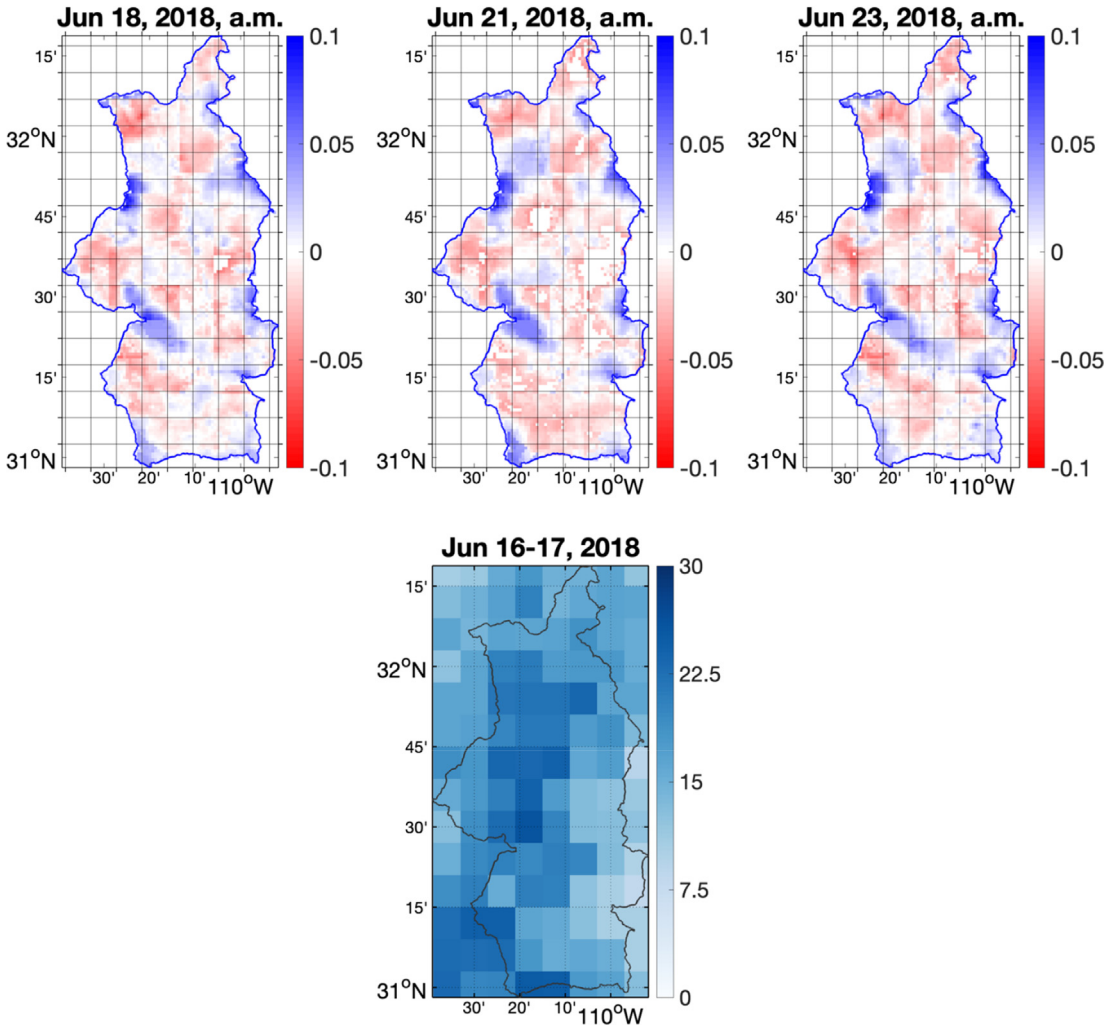

Fig. 7. (*continued*)

$$m = \frac{\sum_{i=1}^{n} \theta_i}{n} \tag{5}$$

where, R^2 and b are the coefficient of determination and bias between *in situ* SM θ and estimated SM $\hat{\theta}$ (1 km downscaled and 9 km SMAP), respectively. ubRMSE is the unbiased RMSE which removes the bias b from $\hat{\theta}$. σ is the spatial standard deviation of estimated or *in situ* SM. m is the averaged SM.

In addition, in order to analyze the non-randomness and the correlation of the data in the time series, the autocorrelation function was applied on all three SM data sets and the autocorrelation R at the lag k is calculated as

$$R_k = \frac{\sum_{i=1}^{N-k} \left(\theta_i - \bar{\theta}\right)\left(\theta_{i+k} - \bar{\theta}\right)}{\sum_{i=1}^{N} \left(\theta_i - \bar{\theta}\right)^2} \tag{6}$$

where, θ_i is the SM estimate on the day i. In this equation, the time variable is not used for calculating the correlation coefficient, but the two SM estimates on the days i and $i + k$ were used instead. Usually, the first correlation when lag = 1 is of interest in practical use.

The first step of the downscaling algorithm was to establish a reliable relationship between θ and ΔT_s using outputs from the NLDAS Noah model between 1981 and 2018, separately for each NDVI-class on a monthly basis. Fig. 3 shows the overall R^2 averaged from all NDVI classes for each NLDAS grid over the San Pedro watershed for the months of April through September, where each grid value represents the average value from the $\theta - \Delta T_s$ linear regression fit of all NDVI classes. The maps demonstrate a change in the $\theta - \Delta T_s$ agreement for the April to September period. Higher R^2 are achieved during the months of June and July. It can be concluded that generally the warm months exhibit a stronger thermal inertia relationship between θ and ΔT_s. June and July had relatively better overall R^2, and most of the grid values in these two months are greater than 0.4. In addition to these, we observe that some grids have relatively lower overall R^2. These areas correspond to complex terrain and higher vegetation coverage, which can lead to higher errors of NLDAS outputs (Hong et al., 2009). Fig. 4 and Table 2 summarize the $\theta - \Delta T_s$ linear regression fit statistics using the data between 1981 and 2018 at 6 locations for the month of July. These results demonstrate generally better R^2 at the San Pedro Basin (R^2 ranges 0.516–0.782) and Tonzi Ranch (R^2 ranges 0.417–0.213) compared to the other sites. It also can be noted that the NDVI range at the San Pedro Basin is the narrowest which is approximately between 0 and 0.3, while the other sites have wider NDVI ranges. In addition, the R^2 computed at the sites located in the western U.S. (i.e., San Pedro Basin, Reynolds Creek, and Tonzi Ranch), where have generally lower vegetation coverage, are generally better than the sites located in the eastern U.S. (i.e., Stillwater, Little River and Ithaca). We may conclude

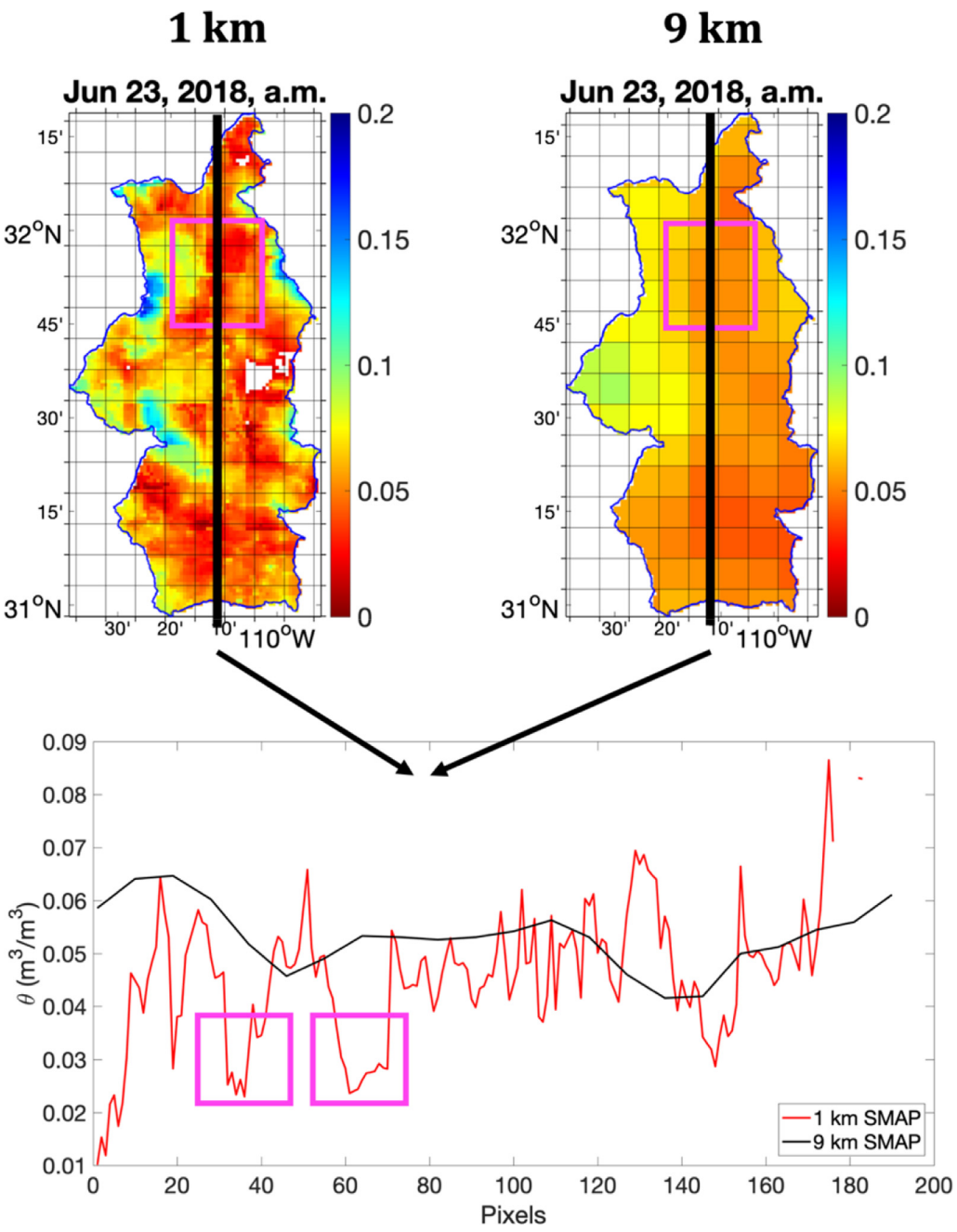

Fig. 8. Comparison between 1 km and 9 km SMAP SM on June 23, 2018. The SM values along the black transection lines proved that the downscaled map captured more SM spatial features than 9 km map. Peaks and dips, which represented SM dry-down and wetting events were better shown on the curve of 1 km SM. Especially, the pink boxes shown that the two dips were captured by 1 km map while 9 km map did not. (For interpretation of the references to colour in this figure legend, the reader is referred to the web version of this article.)

that the vegetation has an influence on the $\theta - \Delta T_s$ relationship. Additionally, the R^2 of the $\theta - \Delta T_s$ relationship does not show a regular descending trend as NDVI increased.

4.2. Downscaled SMAP SM results

The 1 km downscaled SMAP SM and the original 9 km SMAP SM are shown in Fig. 5. Maps represent 8-day composites generated using SM estimates from the ascending and the descending overpasses separately between June 1 and 16, 2018 over the CONUS domain. The 1 km SM maps display similar patterns as the 9 km SM maps, but with greater detail. The 1 km SM maps have missing spatial coverage, which is due to the removal of cloud-contaminated pixels from the MODIS products, the removal of low-quality pixels, as well as the gaps between the swaths of the MODIS and the SMAP products. From the Fig. 6a, when compared the average number of days between 2015 and 2018 which have both ISMN and 9 km SMAP SM data with the average number of days which have no 1 km SMAP SM data, it is found that the ratio between ISMN/9 km availability and 1 km SM unavailability is approximately 2:3 for three networks: COSMOS, SCAN and USCRN, while this ratio is approximately 1:3 for SoilSCAPE. From the Fig. 6b, if analyzed regarding the source of the missing days of the 1 km downscaled SMAP SM data, the MODIS LST data approximately account for 65% of missing days, while the 9 km SMAP data approximately account for the remaining 35%.

Fig. 7a-b shows maps of the 1 km downscaled and 9 km SMAP SM,

Table 3
a-b. Statistical variables R^2, unbiased RMSE, bias, p-value and confidence interval at significance level of 0.05 from the validations of (a) 1 km downscaled and (b) 9 km SMAP radiometer SM estimates of descending overpass by ISMN *in situ* measurements between 2015 and 2018 from 100 validation sites in CONUS, including sites from the networks COSMOS, SCAN, SoilSCAPE, and USCRN.

Site Name	Network	Number	R^2	ubRMSE	bias	p-value	Confidence interval
ARM-1	COSMOS	92	0.584	0.022	−0.017	0.000	0.229
Fort Peck	COSMOS	116	0.525	0.010	0.007	0.000	0.235
Kendall	COSMOS	23	0.637	0.022	0.023	0.000	0.283
Lower Salt Creek	COSMOS	103	0.104	0.025	0.007	0.001	0.162
Lucky Hills	COSMOS	24	0.594	0.021	0.021	0.000	0.434
Manitou Forest Ground	COSMOS	87	0.421	0.022	−0.008	0.000	0.134
Marshall Colorado	COSMOS	115	0.651	0.011	0.007	0.000	0.140
Metolius	COSMOS	186	0.415	0.022	0.001	0.000	0.085
Reynolds Creek	COSMOS	150	0.585	0.031	0.026	0.000	0.095
SMAP-OK	COSMOS	79	0.671	0.006	0.005	0.000	0.171
Santa Rita Criosote	COSMOS	103	0.729	0.024	−0.024	0.000	0.149
Santa Rita Mesquite	COSMOS	26	0.790	0.014	−0.005	0.000	0.382
Soaproot	COSMOS	62	0.540	0.031	−0.011	0.000	0.107
Tonzi Ranch	COSMOS	165	0.702	0.018	0.017	0.000	0.086
Abrams	SCAN	116	0.220	0.007	0.004	0.000	0.460
Bragg Farm	SCAN	83	0.491	0.018	0.003	0.000	0.141
Cave Valley	SCAN	75	0.326	0.023	−0.023	0.000	0.320
Deep Springs	SCAN	180	0.168	0.032	0.025	0.000	0.123
Desert Center	SCAN	58	0.127	0.017	−0.007	0.006	0.186
Dexter	SCAN	83	0.395	0.007	0.006	0.000	0.292
Enterprise	SCAN	185	0.428	0.009	0.003	0.000	0.127
Essex	SCAN	110	0.242	0.031	−0.014	0.000	0.074
Ford Dry Lake	SCAN	52	0.212	0.018	0.000	0.001	0.170
Fort Assiniboine #1	SCAN	174	0.682	0.025	−0.012	0.000	0.090
Grouse Creek	SCAN	82	0.655	0.021	−0.005	0.000	0.133
Hals Canyon	SCAN	69	0.417	0.016	−0.001	0.000	0.205
Holden	SCAN	159	0.600	0.016	−0.008	0.000	0.190
Knox City	SCAN	118	0.503	0.011	−0.006	0.000	0.186
Levelland	SCAN	83	0.370	0.005	−0.001	0.000	0.279
Lind #1	SCAN	169	0.690	0.013	−0.001	0.000	0.072
Los Lunas Pmc	SCAN	154	0.133	0.021	−0.003	0.000	0.179
Lovelock Nnr	SCAN	139	0.524	0.021	−0.021	0.000	0.156
Mammoth Cave	SCAN	98	0.479	0.033	−0.004	0.000	0.113
Marble Creek	SCAN	150	0.236	0.022	−0.017	0.000	0.148
Mason #1	SCAN	83	0.472	0.019	−0.018	0.000	0.252
Mcalister Farm	SCAN	81	0.772	0.034	−0.002	0.000	0.071
North Issaquena	SCAN	67	0.183	0.033	0.031	0.000	0.398
Price	SCAN	126	0.371	0.028	−0.027	0.000	0.206
Sand Hollow	SCAN	129	0.371	0.024	−0.022	0.000	0.189
Scott	SCAN	68	0.398	0.012	0.007	0.000	0.250
Sevilleta	SCAN	88	0.356	0.027	−0.010	0.000	0.110
Spooky	SCAN	138	0.217	0.013	−0.012	0.000	0.247
Torrington #1	SCAN	112	0.476	0.021	−0.020	0.000	0.165
UAPB Point Remove	SCAN	118	0.420	0.014	−0.012	0.000	0.172
Vermillion	SCAN	197	0.147	0.030	−0.017	0.000	0.104
Walnut Gulch #1	SCAN	104	0.700	0.019	0.011	0.000	0.101
node1019	SOILSCAPE	45	0.877	0.028	−0.026	0.000	0.167
node1023	SOILSCAPE	46	0.799	0.026	−0.022	0.000	0.120
node1403	SOILSCAPE	11	0.613	0.024	0.004	0.074	0.481
node1500	SOILSCAPE	35	0.601	0.025	0.025	0.000	0.244
node1506	SOILSCAPE	17	0.878	0.013	−0.009	0.000	0.219
node401	SOILSCAPE	113	0.751	0.032	0.028	0.000	0.073
node402	SOILSCAPE	108	0.708	0.015	−0.015	0.000	0.175
node404	SOILSCAPE	60	0.818	0.018	−0.012	0.000	0.118
node405	SOILSCAPE	113	0.644	0.017	−0.011	0.000	0.095
node406	SOILSCAPE	112	0.729	0.026	0.008	0.000	0.065
node408	SOILSCAPE	113	0.799	0.028	−0.018	0.000	0.057
node410	SOILSCAPE	54	0.783	0.030	−0.029	0.000	0.126
node412	SOILSCAPE	113	0.761	0.027	0.024	0.000	0.078
node413	SOILSCAPE	107	0.821	0.011	0.006	0.000	0.071
node414	SOILSCAPE	52	0.840	0.026	−0.022	0.000	0.088
node415	SOILSCAPE	111	0.721	0.017	0.006	0.000	0.078
node416	SOILSCAPE	106	0.756	0.020	0.001	0.000	0.069
node502	SOILSCAPE	50	0.792	0.018	0.013	0.000	0.112
node504	SOILSCAPE	117	0.693	0.024	0.019	0.000	0.085
node508	SOILSCAPE	33	0.681	0.021	0.011	0.000	0.172
node513	SOILSCAPE	118	0.668	0.033	0.013	0.000	0.062
node517	SOILSCAPE	40	0.780	0.026	0.004	0.000	0.138
node710	SOILSCAPE	40	0.793	0.033	−0.029	0.000	0.199
node900	SOILSCAPE	47	0.707	0.030	−0.022	0.000	0.131
node901	SOILSCAPE	83	0.692	0.020	−0.018	0.000	0.126
node902	SOILSCAPE	42	0.789	0.005	−0.005	0.000	0.159

(*continued on next page*)

Table 3 (*continued*)

Site Name	Network	Number	R^2	ubRMSE	bias	p-value	Confidence interval
node905	SOILSCAPE	82	0.711	0.023	−0.001	0.000	0.091
node906	SOILSCAPE	82	0.652	0.033	−0.027	0.000	0.111
node909	SOILSCAPE	83	0.798	0.016	−0.013	0.000	0.091
node910	SOILSCAPE	20	0.425	0.014	−0.002	0.002	0.366
node911	SOILSCAPE	83	0.656	0.021	−0.012	0.000	0.112
node912	SOILSCAPE	82	0.738	0.024	0.020	0.000	0.103
node913	SOILSCAPE	83	0.771	0.017	0.009	0.000	0.090
node914	SOILSCAPE	40	0.574	0.020	−0.018	0.000	0.220
node916	SOILSCAPE	55	0.644	0.023	−0.005	0.000	0.134
Baker 5W	USCRN	153	0.301	0.013	−0.011	0.000	0.176
Bowling Green 21 NNE	USCRN	90	0.548	0.024	0.023	0.000	0.153
Bronte 11 NNE	USCRN	144	0.518	0.031	−0.031	0.000	0.175
Corvallis 10 SSW	USCRN	170	0.772	0.021	−0.021	0.000	0.085
Elgin 5 S	USCRN	111	0.463	0.012	−0.008	0.000	0.152
Fallbrook 5 NE	USCRN	124	0.360	0.008	−0.004	0.000	0.162
John Day 35 WNW	USCRN	163	0.561	0.028	−0.027	0.000	0.126
Medora 7 E	USCRN	123	0.525	0.011	−0.004	0.000	0.131
Mercury 3 SSW	USCRN	101	0.149	0.011	−0.008	0.000	0.236
Monahans 6 ENE	USCRN	152	0.461	0.016	−0.016	0.000	0.256
Nunn 7 NNE	USCRN	113	0.666	0.029	−0.028	0.000	0.161
Panther Junction 2N	USCRN	98	0.318	0.030	0.021	0.000	0.127
Riley 10 WSW	USCRN	112	0.577	0.016	0.011	0.000	0.120
Sandstone 6W	USCRN	114	0.309	0.025	−0.024	0.000	0.217
Socorro 20N	USCRN	121	0.158	0.026	0.006	0.000	0.213
Stillwater 5 WNW	USCRN	122	0.768	0.013	0.005	0.000	0.081
Stovepipe Wells 1 SW	USCRN	103	0.510	0.019	−0.019	0.000	0.325
Tucson 11W	USCRN	177	0.515	0.026	−0.024	0.000	0.083
Whitman 5 ENE	USCRN	149	0.458	0.011	−0.011	0.000	0.163
ARM-1	COSMOS	92	0.558	0.023	−0.018	0.000	0.239
Fort Peck	COSMOS	116	0.642	0.012	−0.001	0.000	0.184
Kendall	COSMOS	23	0.555	0.023	0.022	0.000	0.332
Lower Salt Creek	COSMOS	103	0.197	0.026	0.002	0.000	0.109
Lucky Hills	COSMOS	24	0.570	0.024	0.024	0.000	0.356
Manitou Forest Ground	COSMOS	87	0.482	0.022	0.003	0.000	0.125
Marshall Colorado	COSMOS	115	0.627	0.026	−0.026	0.000	0.107
Metolius	COSMOS	186	0.209	0.031	0.003	0.000	0.088
Reynolds Creek	COSMOS	150	0.562	0.021	0.016	0.000	0.077
SMAP-OK	COSMOS	79	0.664	0.031	−0.030	0.000	0.180
Santa Rita Criosote	COSMOS	103	0.564	0.020	−0.019	0.000	0.090
Santa Rita Mesquite	COSMOS	26	0.724	0.015	−0.014	0.000	0.246
Soaproot	COSMOS	62	0.463	0.033	0.017	0.000	0.098
Tonzi Ranch	COSMOS	165	0.684	0.031	0.027	0.000	0.062
Abrams	SCAN	116	0.202	0.018	0.015	0.000	0.438
Bragg Farm	SCAN	83	0.533	0.020	0.001	0.000	0.137
Cave Valley	SCAN	75	0.376	0.067	−0.067	0.000	0.232
Deep Springs	SCAN	180	0.130	0.032	0.020	0.000	0.086
Desert Center	SCAN	58	0.180	0.036	−0.032	0.001	0.137
Dexter	SCAN	83	0.496	0.021	0.015	0.000	0.290
Enterprise	SCAN	185	0.455	0.017	−0.009	0.000	0.093
Essex	SCAN	110	0.137	0.040	−0.027	0.000	0.075
Ford Dry Lake	SCAN	52	0.201	0.026	−0.017	0.001	0.154
Fort Assiniboine #1	SCAN	174	0.556	0.024	0.005	0.000	0.068
Grouse Creek	SCAN	82	0.512	0.031	−0.022	0.000	0.092
Hals Canyon	SCAN	69	0.263	0.025	−0.020	0.000	0.146
Holden	SCAN	159	0.263	0.031	−0.029	0.000	0.078
Knox City	SCAN	118	0.478	0.017	−0.017	0.000	0.148
Levelland	SCAN	83	0.316	0.009	−0.008	0.000	0.241
Lind #1	SCAN	169	0.683	0.017	−0.006	0.000	0.064
Los Lunas Pmc	SCAN	154	0.094	0.040	0.029	0.000	0.126
Lovelock Nnr	SCAN	139	0.370	0.023	−0.016	0.000	0.109
Mammoth Cave	SCAN	98	0.504	0.030	−0.013	0.000	0.124
Marble Creek	SCAN	150	0.104	0.032	−0.023	0.000	0.105
Mason #1	SCAN	83	0.485	0.106	−0.106	0.000	0.221
Mcalister Farm	SCAN	81	0.781	0.036	−0.002	0.000	0.066
North Issaquena	SCAN	67	0.155	0.020	0.015	0.001	0.392
Price	SCAN	126	0.052	0.265	−0.051	0.000	0.143
Sand Hollow	SCAN	129	0.042	0.192	−0.041	0.000	0.134
Scott	SCAN	68	0.024	0.395	0.022	0.000	0.247
Sevilleta	SCAN	88	0.028	0.326	0.006	0.000	0.113
Spooky	SCAN	138	0.216	0.032	−0.031	0.000	0.186
Torrington #1	SCAN	112	0.467	0.027	−0.026	0.000	0.156
UAPB Point Remove	SCAN	118	0.408	0.012	−0.009	0.000	0.172
Vermillion	SCAN	197	0.107	0.035	−0.026	0.000	0.099
Walnut Gulch #1	SCAN	104	0.614	0.020	0.006	0.000	0.072
node1019	SOILSCAPE	45	0.841	0.019	0.018	0.000	0.124

(*continued on next page*)

Table 3 (*continued*)

Site Name	Network	Number	R^2	ubRMSE	bias	p-value	Confidence interval
node1023	SOILSCAPE	46	0.757	0.030	0.023	0.000	0.092
node1403	SOILSCAPE	11	0.312	0.025	0.022	0.004	0.400
node1500	SOILSCAPE	35	0.649	0.020	0.017	0.000	0.186
node1506	SOILSCAPE	17	0.775	0.017	−0.012	0.000	0.141
node401	SOILSCAPE	113	0.696	0.046	0.038	0.000	0.055
node402	SOILSCAPE	108	0.693	0.026	−0.024	0.000	0.123
node404	SOILSCAPE	60	0.762	0.026	−0.026	0.000	0.097
node405	SOILSCAPE	113	0.635	0.022	0.000	0.000	0.069
node406	SOILSCAPE	112	0.679	0.040	0.017	0.000	0.048
node408	SOILSCAPE	113	0.747	0.034	−0.008	0.000	0.044
node410	SOILSCAPE	54	0.723	0.025	−0.018	0.000	0.096
node412	SOILSCAPE	113	0.689	0.041	0.034	0.000	0.061
node413	SOILSCAPE	107	0.752	0.027	0.017	0.000	0.058
node414	SOILSCAPE	52	0.777	0.029	−0.011	0.000	0.071
node415	SOILSCAPE	111	0.689	0.031	0.015	0.000	0.057
node416	SOILSCAPE	106	0.699	0.033	0.011	0.000	0.053
node502	SOILSCAPE	50	0.772	0.054	0.050	0.000	0.085
node504	SOILSCAPE	117	0.662	0.024	−0.020	0.000	0.075
node508	SOILSCAPE	33	0.679	0.033	−0.031	0.000	0.142
node513	SOILSCAPE	118	0.650	0.061	0.051	0.000	0.055
node517	SOILSCAPE	40	0.597	0.063	0.057	0.000	0.088
node710	SOILSCAPE	40	0.525	0.013	−0.004	0.000	0.116
node900	SOILSCAPE	47	0.590	0.052	0.036	0.000	0.115
node901	SOILSCAPE	83	0.697	0.038	0.034	0.000	0.092
node902	SOILSCAPE	42	0.694	0.055	0.053	0.000	0.146
node905	SOILSCAPE	82	0.640	0.063	0.052	0.000	0.075
node906	SOILSCAPE	82	0.678	0.038	0.026	0.000	0.078
node909	SOILSCAPE	83	0.766	0.045	0.039	0.000	0.072
node910	SOILSCAPE	20	0.754	0.041	0.037	0.000	0.160
node911	SOILSCAPE	83	0.641	0.049	0.040	0.000	0.084
node912	SOILSCAPE	82	0.684	0.077	0.073	0.000	0.082
node913	SOILSCAPE	83	0.772	0.066	0.061	0.000	0.066
node914	SOILSCAPE	40	0.533	0.045	0.037	0.000	0.140
node916	SOILSCAPE	55	0.547	0.062	0.050	0.000	0.112
Baker 5W	USCRN	153	0.488	0.039	−0.038	0.000	0.107
Bowling Green 21 NNE	USCRN	90	0.507	0.025	0.024	0.000	0.169
Bronte 11 NNE	USCRN	144	0.682	0.039	−0.038	0.000	0.129
Corvallis 10 SSW	USCRN	170	0.831	0.019	−0.009	0.000	0.054
Elgin 5 S	USCRN	111	0.506	0.019	−0.014	0.000	0.120
Fallbrook 5 NE	USCRN	124	0.144	0.012	0.000	0.000	0.199
John Day 35 WNW	USCRN	163	0.476	0.048	−0.046	0.000	0.099
Medora 7 E	USCRN	123	0.489	0.015	−0.008	0.000	0.134
Mercury 3 SSW	USCRN	101	0.136	0.023	−0.020	0.000	0.171
Monahans 6 ENE	USCRN	152	0.302	0.019	−0.019	0.000	0.173
Nunn 7 NNE	USCRN	113	0.568	0.050	−0.050	0.000	0.150
Panther Junction 2N	USCRN	98	0.486	0.021	−0.001	0.000	0.086
Riley 10 WSW	USCRN	112	0.504	0.020	0.012	0.000	0.121
Sandstone 6W	USCRN	114	0.305	0.043	−0.043	0.000	0.224
Socorro 20N	USCRN	121	0.110	0.027	0.017	0.000	0.131
Stillwater 5 WNW	USCRN	122	0.760	0.014	−0.006	0.000	0.080
Stovepipe Wells 1 SW	USCRN	103	0.268	0.043	−0.043	0.000	0.173
Tucson 11W	USCRN	177	0.507	0.030	−0.028	0.000	0.082
Whitman 5 ENE	USCRN	149	0.502	0.009	−0.009	0.000	0.161

the difference between the 1 km/9 km SM from June 18, 21, and 23, 2018, as well as the accumulated GPM precipitation between June 16 – 17. Please note that it was the only rainfall event that occurred before or during the time period June 18–23 over the San Pedro watershed. A linearly shaped wet area in the middle of the watershed from north to south that is shown in all three 1 km maps which represents the San Pedro River. Furthermore, there are some wet areas (outlined in pink boxes) near the edge of the watershed boundaries that are only captured in the 1 km maps. The difference maps between the 1 km and the 9 km SM also confirm that more spatial variability is present in the downscaled SM product. In addition, the difference maps show that the 1 km SM estimates are lower than the original 9 km product along the edges of the watershed. The corresponding areas that received more precipitation exhibit a slower SM dry down trend. If we draw a transect line vertically across the center of the watershed to compare the 1 km downscaled SM with 9 km SM (Fig. 8), it appears that the 1 km SM line shows greater variability than the 9 km line. Additionally, two SM dry downs can be noted in the line plot, which are located in the north central of the watershed (shown in the pink boxes) from 1 km SM map, while they are completely missing in the 9 km map.

4.3. Validation

The validation metrics, R^2, unbiased RMSE, bias for the 1 km downscaled and the 9 km SMAP SM validations using the ISMN *in situ* measurements are shown in Table 3.

The SoilSCAPE is a soil moisture network with high-density nodes, and the SM sensors are clustered in groups within a relatively small area (1 km^2). (Moghaddam et al., 2010). The network uses Decagon EC-5 capacitance probes to estimate SM at different depths from the series of stations within the Tonzi, California, in northern California (Ford and Quiring, 2019). On the other hand, the COSMOS SM measurements are recorded by cosmic-ray probes from the wireless sensor network (SoilNET) and the best overall accuracy is within 0.013 m^3/m^3 at

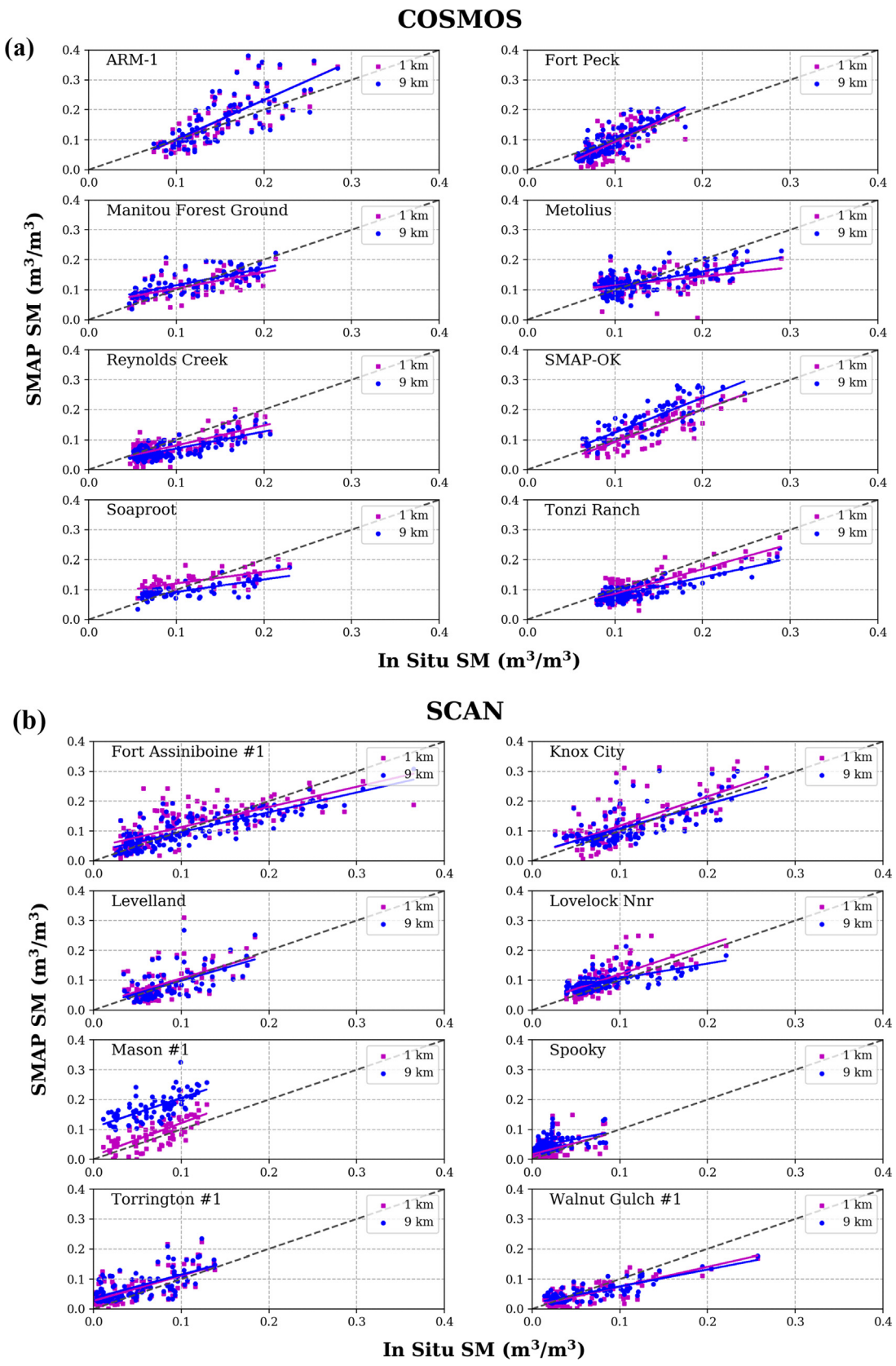

Fig. 9. Validation scatterplots of 1 km/9 km SMAP L2 SM of descending overpass between 2015 and 2018 at 32 ISMN stations. The SMAP SM were validated by ISMN *in situ* measurements from 4 SM networks including (a) COSMOS, (b) SCAN, (c) SoilSCAPE and (d) USCRN.

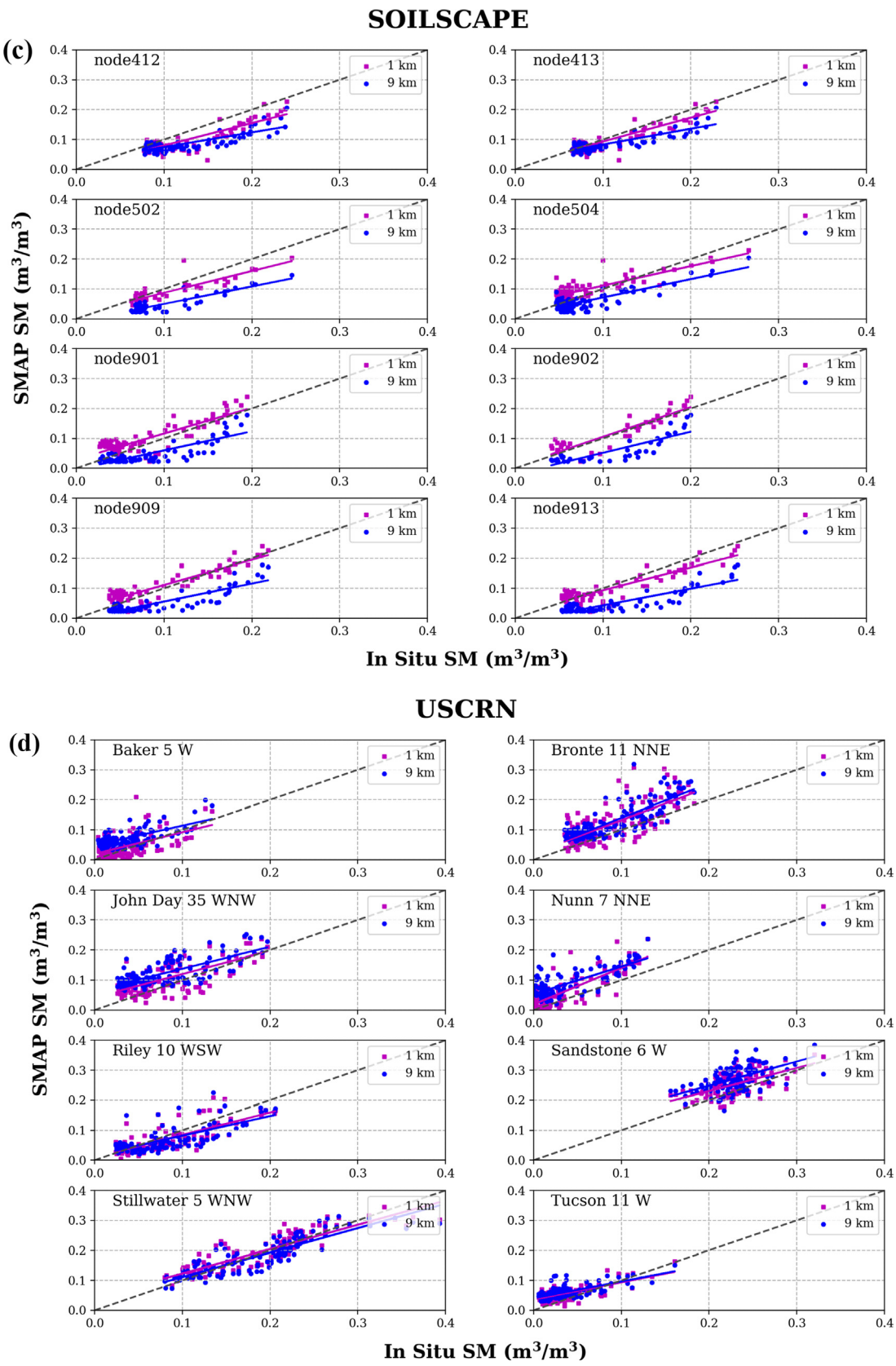

Fig. 9. (*continued*)

regions with low soil water content (Zreda et al., 2012; Bogena et al., 2013; Han et al., 2014; Jakobi et al., 2018). The USCRN uses three sets of probes for soil and climate measurements for minimizing the measurement errors and soil effects. It has an average error of approximately $0.012\,m^3/m^3$ by the triple collocation validation method. However, the largest error was noted at shallower depths (Diamond et al., 2013; Bell et al., 2013a,b; Coopersmith et al., 2016). Lastly, the SCAN uses Stevens Hydraprobe dielectric reflectometers at

Table 4
The average and spatial standard deviation σ from the ISMN *in situ* SM measurements, 1 km downscaled and 9 km SMAP SM between 2015 and 2018 from the 4 sites: Tonzi Ranch, San Pedro River Basin, Oklahoma, and Colorado River Basin.

SM Network	Average			Spatial standard deviation		
	ISMN (Dsc.)	1 km SMAP (Dsc.)	9 km SMAP (Dsc.)	ISMN (Dsc.)	1 km SMAP (Dsc.)	9 km SMAP (Dsc.)
Tonzi Ranch	0.111	0.118	0.096	0.025	0.016	0.011
San Pedro River Basin	0.061	0.062	0.078	0.022	0.017	0.014
Oklahoma	0.180	0.176	0.195	0.035	0.032	0.028
Colorado River Basin	0.078	0.094	0.108	0.044	0.040	0.035

different depths and has hourly intervals (Cosh et al., 2004; Schaefer et al., 2007). Previous studies reported that overall high errors were greater than 0.015 m^3/m^3 at the stations in the eastern CONUS region and Utah agricultural valleys and lowlands (Dirmeyer et al., 2016; Ford and Quiring, 2019).

For the R^2 of 1 km SM, the SoilSCAPE network has the highest average value (0.728) compared to the other networks. The average R^2 values for COSMOS, SCAN and USCRN are 0.568, 0.399 and 0.470, respectively. The average ubRMSE for all 4 networks range between 0.02 and 0.022 m^3/m^3 and they do not show much difference. For the average bias, the COSMOS has the best result (0.003 m^3/m^3), while the other three networks SCAN, SoilSCAPE and USCRN have -0.005, -0.004 and -0.009 m^3/m^3, respectively. The relatively higher bias at the USCRN is most likely due to the fact that some stations are located in farmland and forest, and the SM measurements are influenced by vegetation cover and undulating terrain, which may cause uncertainties in the 1 km / 9 km SM estimates. Comparing the validation metrics of the 1 km SM to the 9 km, on average, the R^2 increases by 0.045, the ubRMSE decreases by 0.018 m^3/m^3, and the bias decreases by 0.001 m^3/m^3, for the 4 SM networks. Given these results, we can conclude that the downscaling algorithm performs better over areas with lower soil moisture content and less complex vegetation conditions. For the p-values of the regression analysis output for each ISMN station, both 1 km/9 km SM validations are much less than 0.05 at the significance level $\alpha = 0.05$, which indicates the significance of the regression fitting. For the 95% confidence interval of the regression, on average, the 1 km SMAP SM is 0.17, while the 9 km SMAP SM is 0.139. The values are relatively narrow and can also prove the accuracy of the regression fitting estimates.

From Table 3, we may also note the improvement in ubRMSE and bias at 1 km validations over 9 km validations for a few stations but have no improvement of R^2. For example, the stations include Fort Peck, Kendall from COSMOS; Bragg Farm, Cave Valley from SCAN; node901, node906 from SoilSCAPE; and Baker 5 W, Bronte 11 NNE from USCRN. This is due to the bias-variance tradeoff issue occurred in 9 km validation, which implies high bias and low variance of the data pairs in the validation plots. This fact especially could be observed in the plots of Fort Peck, node-901, Bronte 11 NNE in Fig. 9a, c and d. The 1 km points are relatively more scattered, but the fit lines are closer to the 1–1 diagonal lines. Moreover, from Fig. 9a-d, it can be observed that the fit lines of 1 km data pairs are generally closer to the diagonal lines than the fit lines of 9 km data pairs for all scatter plots, which indicates the improved accuracy of the 1 km downscaled SM. Additionally, it is observed that the underestimation occurred for 9 km SMAP SM for most of the stations from COSMOS, SCAN, and SoilSCAPE, while the overestimation occurred in USCRN. We also can find that the underestimation trend of SM occurred in some stations from the western U.S., including such as Walnut Gulch #1, Tonzi Ranch and Reynolds Creek (Fig. 9a, b), while the overestimation trend occurred in stations from Eastern U.S., including Bronte 11 NNE and SMAP-OK (Fig. 9a, d). The overestimation/underestimation trends of 9 km data pairs are clearly reduced in 1 km data pairs, especially in the stations SMAP-OK (Fig. 9a), Mason #1 (Fig. 9b), and node901 (Fig. 9c).

Table 4 shows the average daily spatial standard deviation σ and average SM values of the 3 data sets: 1 km, 9 km SMAP SM and ISMN SM from the 4 sites between 2015 and 2018. The σ refers to the spatial variability of SM. It can be summarized that, on average, the σ of 1 km SM is 0.026 m^3/m^3, while 9 km SM is 0.022 m^3/m^3 for all 4 sites. The difference of σ between 1 km and ISMN is 0.005 m^3/m^3 on average. It is clearly less than the difference of σ between 9 km and ISMN, which is 0.01 m^3/m^3 on average. This indicates that the 1 km downscaled SM can better estimate the spatial variability than the 9 km SM. For the average SM, the 1 km is 0.113 m^3/m^3 on average and has an average difference of 0.005 m^3/m^3 with the ISMN, while the 9 km is 0.119 m^3/m^3 and has an average difference of 0.012 m^3/m^3 with the ISMN. It is also summarized that the 1 km SM average is overall closer to the ISMN SM.

From the time series plots between the averaged 1 km, 9 km, ISMN SM data and GPM precipitation at the 4 SM networks between 2015 and 2018 shown in Fig. 10a-d, we may note that the 1 km/9 km SM estimates had a good agreement with ISMN data during the days without rain. On the days with precipitation, we observe greater SM temporal variability and difference between estimated SM and ISMN SM, which agreed with our conclusion made in the above paragraph that the precipitation could affect the accuracy of estimated SM. For example, the difference between ISMN and 1 km/9 km SMAP SM during rainy days can be observed in the following stations: ARM-1 and Fort peck in 2016, SMAP-OK in 2017 (Fig. 10a); Mason #1 (Fig. 10b), Sandstone 6 W and Stillwater 5 WNW (Fig. 10d) in all 4 years. The 1 km downscaled SM estimates of some days with precipitation were missing, which was due to the cloud cover in MODIS images. On the other hand, it is found that the 1 km SMAP SM generally better agreed to ISMN SM than 9 km SM for all sites, especially during the rainy days. Table 5 shows the time-series autocorrelation R (lag = 1) of the 1 km, 9 km SMAP SM and the corresponding ISMN SM measurements of descending overpass between 2015 and 2018 from 100 ISMN validations stations of 4 SM networks. If the stations are grouped by the networks, it can be summarized that, on average, the R for ISMN SM is 0.888, comparing with R = 0.791 for 1 km SM and R = 0.741 for 9 km SM. The results prove that both 1 km and 9 km SM have strong autocorrelation of 1-day lag. From Fig. 11a-c, the time-series autocorrelations for all three stations show descending trends as the lag increases. On the other hand, the R of ISMN data decreases more slowly than either 1 km or 9 km SMAP SM as the lag increases. If observed the shaded area which represents the confident interval, the 1 km and 9 km SM both have good autocorrelations when lag $<$ 4 for the Tonzi Ranch station, while the other two stations show good autocorrelations when lag $<$ 2.

5. Conclusions and discussion

In this paper, we modified and implemented a 1 km SM downscaling algorithm, which was based on the thermal inertia relationship between surface temperature difference and SM under different vegetation conditions. The approach was used to downscale the SMAP enhanced L2 radiometer only half-orbit 9 km daily SM retrievals over the CONUS during the growing season between April and September from 2015 to 2018. The downscaling algorithm was developed and implemented using remote sensing and LSM derived variables, which were readily

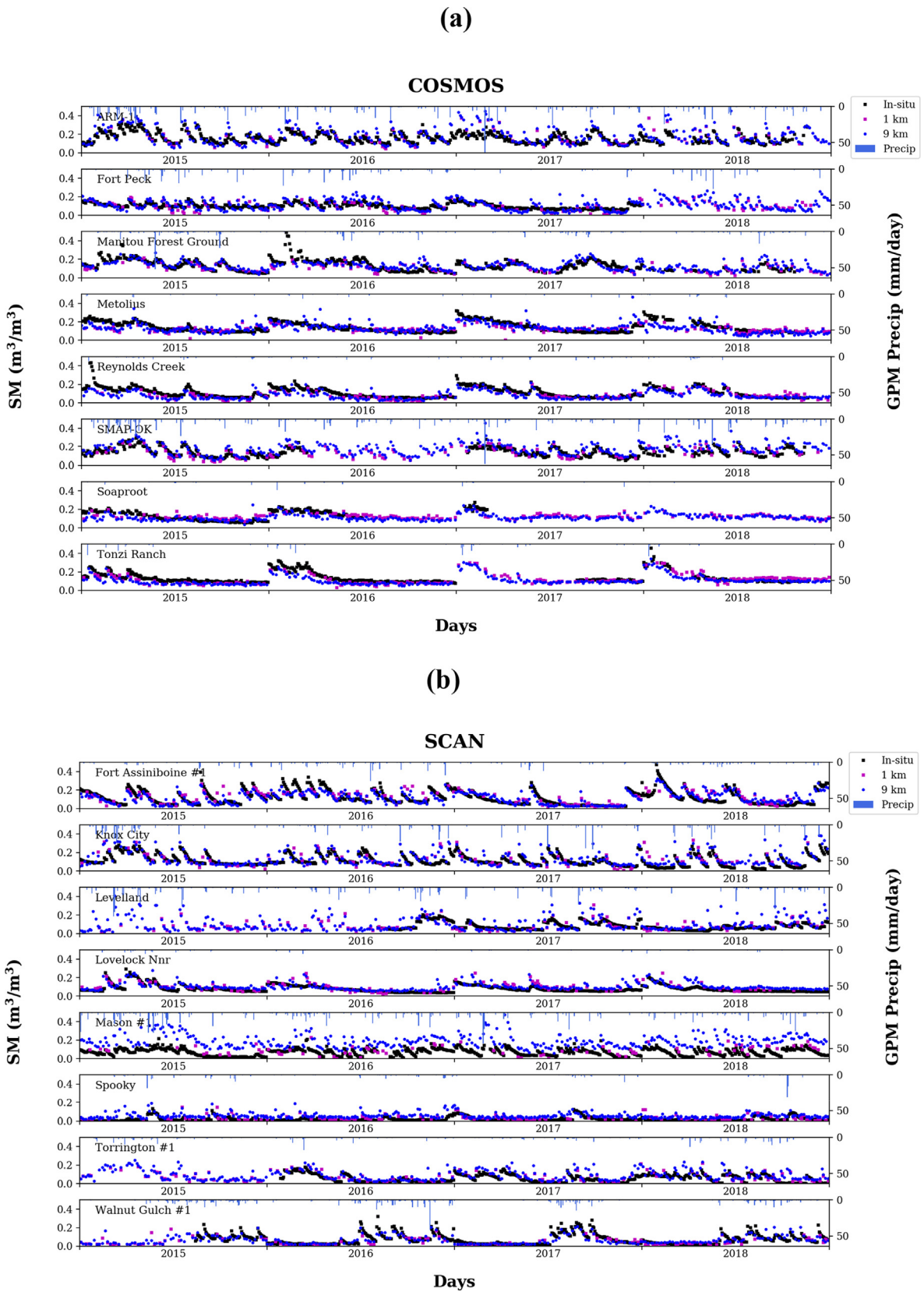

Fig. 10. Time-series plots of the averaged 1 km/9 km SMAP SM estimates and corresponding ISMN *in situ* SM measurements of descending overpass of 64 stations from 4 SM networks, including (a) COSMOS, (b) SCAN, (c) SoilSCAPE and (d) USCRN. The blue bars represent 10 km daily GPM-IMERG L3 precipitation corresponding to each site. (For interpretation of the references to colour in this figure legend, the reader is referred to the web version of this article.)

(c)

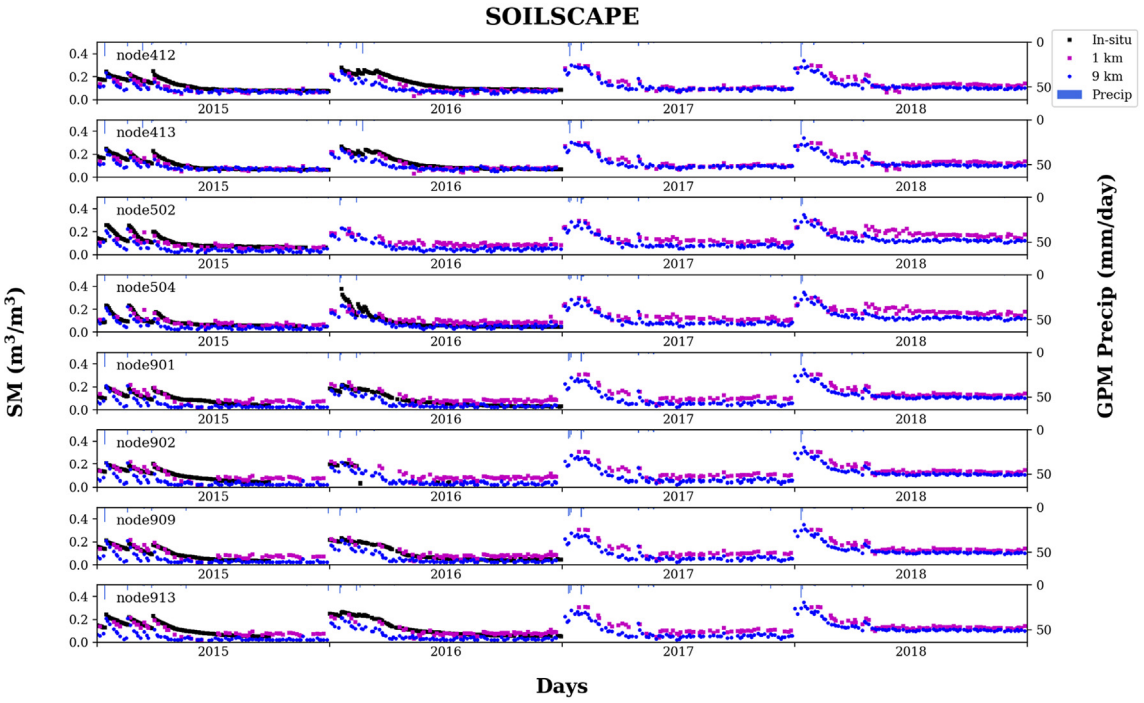

(d)

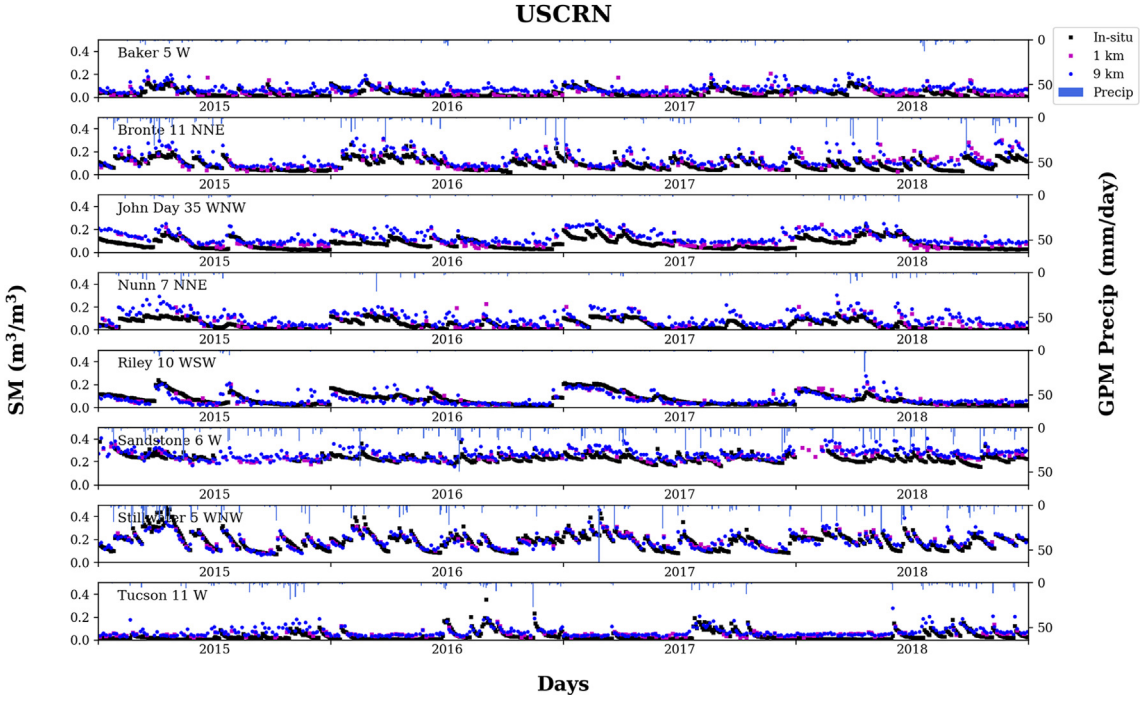

Fig. 10. (*continued*)

available every 2 ~ 3 days. A major revision to the original algorithm involved downscaling the 9 km SMAP SM by applying the $\theta - \Delta T_s$ model output SM at the native SMAP T_B domain of 33 km. This step could effectively reduce the sharp edge issue that occurred in the downscaled SM product which was most likely caused by the errors from the model building and implementation data from NLDAS and MODIS. The algorithm performance and accuracy of the downscaled product were assessed using the ISMN *in situ* SM observations. The performance of the $\theta - \Delta T_s$ model varied in different seasons when analyzing the averaged R^2 from the linear regression best fit of the $\theta - \Delta T_s$ at San Pedro watershed. Warm months (May to July) had higher R^2. The sites from ISMN representing different moisture or vegetation cover conditions were selected for studying and validating the spatial and temporal SM characteristics at 1 km downscaled and 9 km

Table 5
The time-series autocorrelation when lag = 1 of 1 km downscaled, 9 km SMAP SM and ISMN SM measurements of descending overpass between 2015 and 2018 from 100 validation sites in CONUS, including sites from the 4 networks COSMOS, SCAN, SoilSCAPE, and USCRN.

Site Name	Network	ISMN	1 km	9 km
ARM-1	COSMOS	0.842	0.998	0.775
Fort Peck	COSMOS	0.846	0.927	0.780
Kendall	COSMOS	0.891	–	–
Lower Salt Creek	COSMOS	0.822	0.670	0.450
Lucky Hills	COSMOS	0.857	–	–
Manitou Forest Ground	COSMOS	0.921	0.905	0.865
Marshall Colorado	COSMOS	0.850	0.703	0.680
Metolius	COSMOS	0.975	0.308	0.698
Reynolds Creek	COSMOS	0.964	0.676	0.884
SMAP-OK	COSMOS	0.839	0.917	0.845
Santa Rita Criosote	COSMOS	0.884	0.810	0.728
Santa Rita Mesquite	COSMOS	0.794	0.855	0.753
Soaproot	COSMOS	0.708	0.751	0.817
Tonzi Ranch	COSMOS	0.847	0.937	0.898
Abrams	SCAN	0.833	0.995	0.783
Bragg Farm	SCAN	0.853	0.967	0.797
Cave Valley	SCAN	0.855	0.695	0.765
Deep Springs	SCAN	0.938	0.753	0.613
Desert Center	SCAN	0.808	0.618	0.496
Dexter	SCAN	0.868	0.990	0.836
Enterprise	SCAN	0.878	0.681	0.771
Essex	SCAN	0.645	0.156	0.476
Ford Dry Lake	SCAN	0.781	–	–
Fort Assiniboine #1	SCAN	0.890	0.937	0.837
Grouse Creek	SCAN	0.972	0.702	0.878
Hals Canyon	SCAN	0.836	0.534	0.788
Holden	SCAN	0.872	0.893	0.805
Knox City	SCAN	0.870	0.942	0.711
Levelland	SCAN	0.945	0.432	0.741
Lind #1	SCAN	0.969	0.907	0.805
Los Lunas Pmc	SCAN	0.883	0.766	0.445
Lovelock Nnr	SCAN	0.964	0.985	0.892
Mammoth Cave	SCAN	0.917	0.833	0.561
Marble Creek	SCAN	0.921	0.770	0.735
Mason #1	SCAN	0.791	0.999	0.731
Mcalister Farm	SCAN	0.848	1.000	0.825
North Issaquena	SCAN	0.897	1.000	0.956
Price	SCAN	0.830	0.145	0.574
Sand Hollow	SCAN	0.793	0.604	0.399
Scott	SCAN	0.919	–	–
Sevilleta	SCAN	0.779	0.283	0.508
Spooky	SCAN	0.908	0.728	0.369
Torrington #1	SCAN	0.924	0.813	0.726
UAPB Point Remove	SCAN	0.774	0.927	0.870
Vermillion	SCAN	0.913	0.698	0.640
Walnut Gulch #1	SCAN	0.789	–	–
node1019	SOILSCAPE	0.999	0.895	0.750
node1023	SOILSCAPE	0.996	0.895	0.750
node1403	SOILSCAPE	0.651	–	–
node1500	SOILSCAPE	0.905	–	–
node1506	SOILSCAPE	0.608	–	–
node401	SOILSCAPE	0.989	0.937	0.898
node402	SOILSCAPE	0.960	0.937	0.898
node404	SOILSCAPE	0.948	0.937	0.898
node405	SOILSCAPE	0.981	0.960	0.898
node406	SOILSCAPE	0.984	0.937	0.898
node408	SOILSCAPE	0.984	0.937	0.898
node410	SOILSCAPE	0.996	0.937	0.898
node412	SOILSCAPE	0.985	0.937	0.898
node413	SOILSCAPE	0.987	0.937	0.898
node414	SOILSCAPE	0.957	0.937	0.898
node415	SOILSCAPE	0.971	0.937	0.898
node416	SOILSCAPE	0.984	0.937	0.898
node502	SOILSCAPE	0.939	0.835	0.882
node504	SOILSCAPE	0.951	0.835	0.882
node508	SOILSCAPE	0.907	0.835	0.882
node513	SOILSCAPE	0.968	0.835	0.882
node517	SOILSCAPE	0.926	0.720	0.882
node710	SOILSCAPE	0.993	0.968	0.882
node900	SOILSCAPE	0.963	0.895	0.729
node901	SOILSCAPE	0.969	0.895	0.729
node902	SOILSCAPE	0.983	0.895	0.729
node905	SOILSCAPE	0.994	0.895	0.729
node906	SOILSCAPE	0.972	0.895	0.729
node909	SOILSCAPE	0.988	0.895	0.729
node910	SOILSCAPE	0.999	0.895	0.729
node911	SOILSCAPE	0.966	0.895	0.729
node912	SOILSCAPE	0.983	0.895	0.729
node913	SOILSCAPE	0.978	0.895	0.729
node914	SOILSCAPE	0.988	0.895	0.729
node916	SOILSCAPE	0.995	0.895	0.729
Baker 5W	USCRN	0.931	0.546	0.796
Bowling Green 21 NNE	USCRN	0.818	0.974	0.556
Bronte 11 NNE	USCRN	0.859	0.815	0.755
Corvallis 10 SSW	USCRN	0.989	0.902	0.975
Elgin 5 S	USCRN	0.900	0.284	0.597
Fallbrook 5 NE	USCRN	0.953	0.826	0.669
John Day 35 WNW	USCRN	0.960	0.942	0.883
Medora 7 E	USCRN	0.909	0.775	0.721
Mercury 3 SSW	USCRN	0.852	0.677	0.598
Monahans 6 ENE	USCRN	0.701	0.420	0.390
Nunn 7 NNE	USCRN	0.971	0.324	0.860
Panther Junction 2N	USCRN	0.837	–	–
Riley 10 WSW	USCRN	0.983	0.908	0.808
Sandstone 6W	USCRN	0.686	0.810	0.616
Socorro 20N	USCRN	0.869	0.560	0.158
Stillwater 5 WNW	USCRN	0.874	0.984	0.848
Stovepipe Wells 1 SW	USCRN	0.844	–	–
Tucson 11W	USCRN	0.796	0.628	0.586
Whitman 5 ENE	USCRN	0.837	0.933	0.718

resolution. From the validation statistics, it was found that the 1 km downscaled SM showed an improvement compared to the 9 km SM, with the overall improvements of 0.045 for R^2, 0.018 m^3/m^3 for ubRMSE and 0.001 m^3/m^3 for bias, respectively. Overall, the p-values in the regression analyses indicated that both the 1 km and 9 km SMAP SM had statistically significant correlations with ISMN SM. Additionally, the difference of spatial standard deviation σ between the 1 km downscaled and ISMN SM was 0.005 m^3/m^3 on average, which was less than the difference of σ between the 9 km and ISMN SM. The validation results, R^2, ubRMSE and bias between ISMN and 1 km/9 km SM did not show much difference in different SM networks. The algorithm produced reliable downscaling SM on the days with no rain and over regions with less vegetation coverage. On the other hand, the time-series autocorrelation coefficient of the 1 km downscaled SM ranged 0.791 at lag = 1, which indicated the strong correlation between adjacent days. The validation results on the 1 km downscaled SMAP SM showed the potential to extend this data to a global scale.

Our review of some other passive microwave SM downscaling algorithms of recent years that are based on the relationships between SM, LST, and vegetation is in Table 6. These algorithms were applied on AMSR-E, SMOS, ESA and SMAP SM products and the statistical results shown that the R^2 ranged 0.057 – 0.72 and RMSE/RMSD (root mean square difference) ranged 0.027 – 0.1 m^3/m^3. Comparing with similar types of studies, the validation results of our downscaling product, of which average R^2 = 0.541 and average ubRMSE = 0.02 m^3/m^3, show fairly good accuracy.

Declaration of Competing Interest

The authors declare that they have no known competing financial interests or personal relationships that could have appeared to influence the work reported in this paper.

Acknowledgements

We gratefully acknowledge the NASA Terrestrial Hydrology

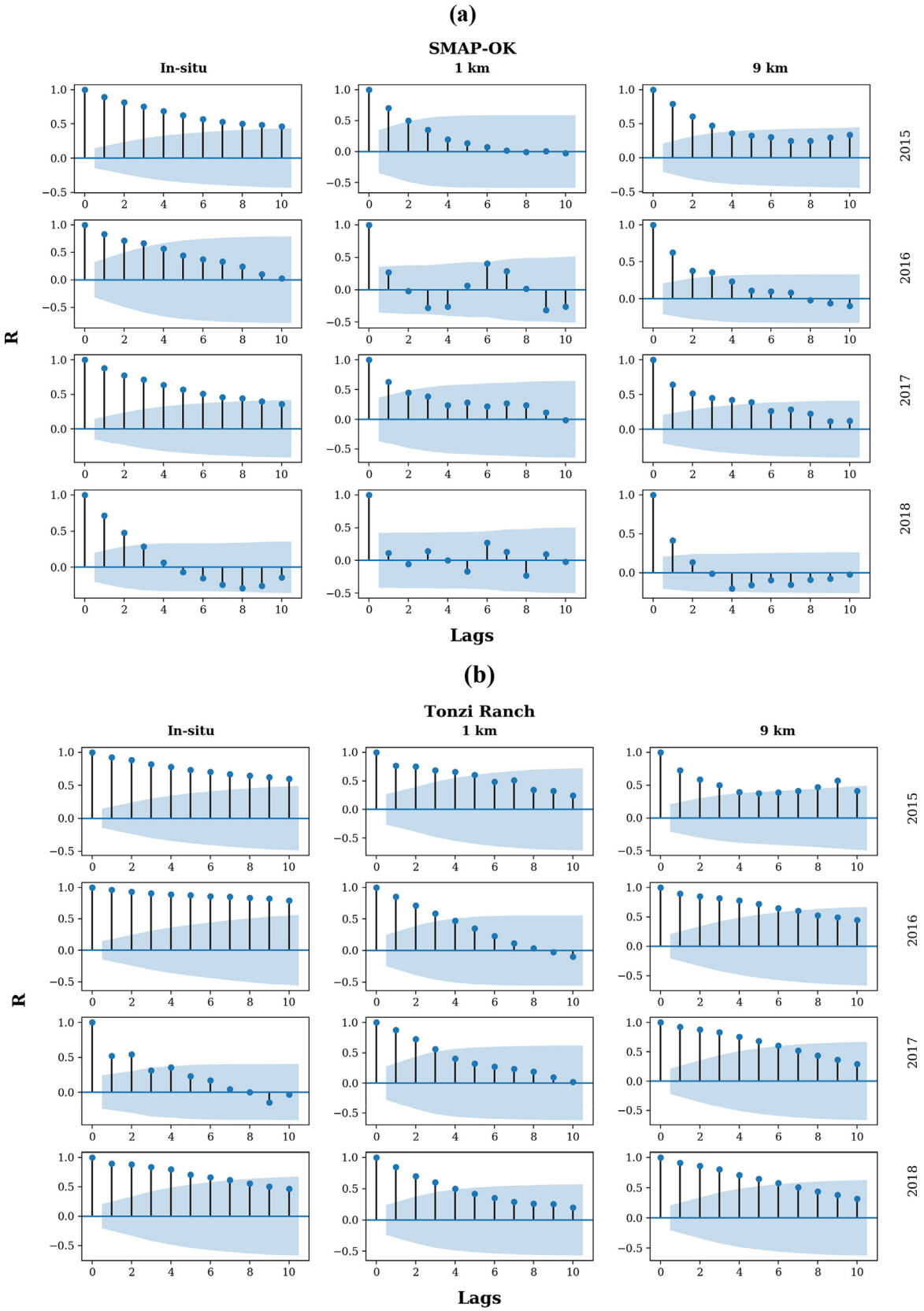

Fig. 11. Time-series autocorrelation plots of the 1 km/9 km SMAP SM estimates and corresponding ISMN *in situ* SM data of descending overpass between 2015 and 2018, at three stations: SMAP-OK, Tonzi Ranch and Bronte 11 NNE. The range of the lag for the autocorrelation function is set between 0 and 10. The shaded area stands for the confidence interval at different lags.

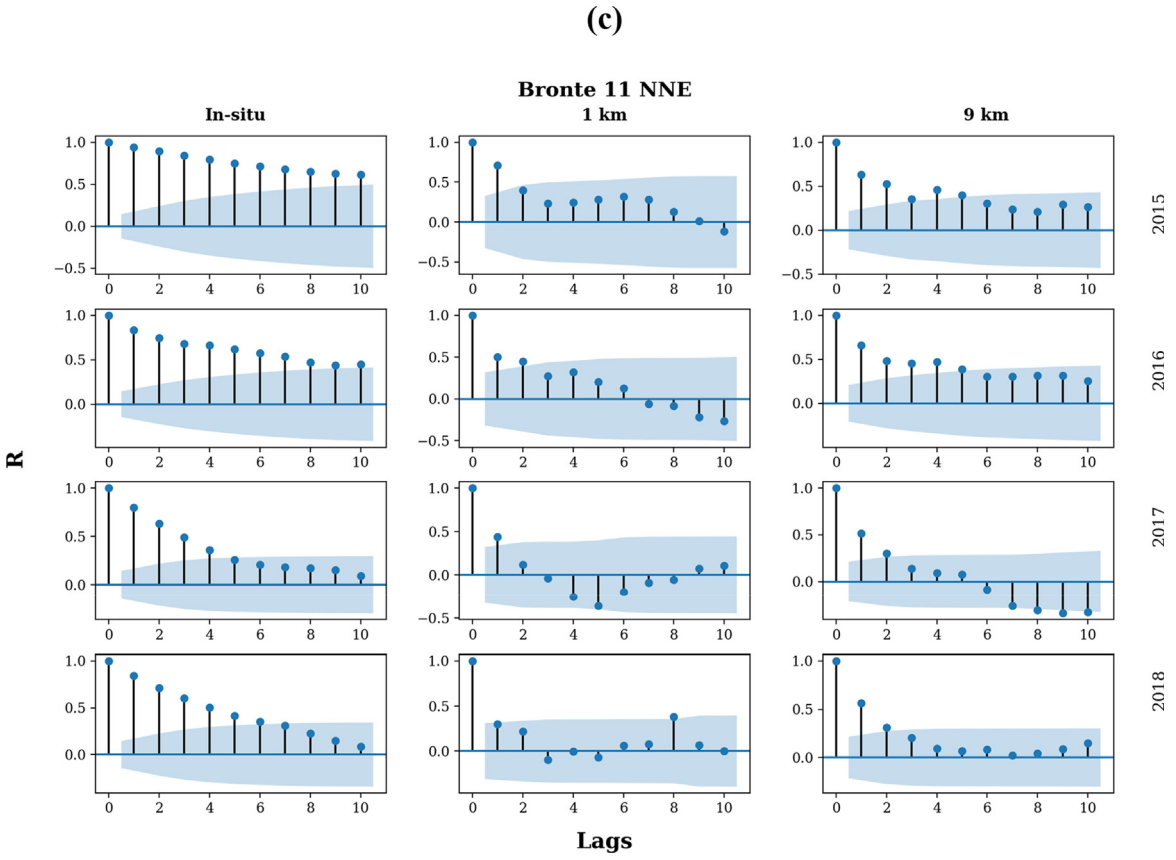

Fig. 11. (*continued*)

Table 6
An overview of the other SM downscaling algorithms that are developed based on the relationships between SM, LST and vegetation.

Authors	Application of the Algorithm	Validation Results
Mallick et al., 2009	AMSR-E C-band product	R^2 = 0.56 and RMSE = 0.027 m^3/m^3 (fraction vegetation cover < 0.5)
Piles et al., 2014	SMOS level-2 product	R^2 = 0.17, ubRMSE = 0.03 m^3/m^3 (descending overpass) R^2 = 0.34, ubRMSE = 0.04 m^3/m^3 (ascending overpass)
Zhao and Li, 2013	LPRM (Land Parameter Retrieval Model) AMSR-E	Average R^2 = 0.057, RMSE = 0.099 m^3/m^3
Merlin et al., 2013	SMOS level-2 product	R^2 = 0.72, RMSE = 0.1 m^3/m^3
Peng et al., 2016	ESA CCI (Climate Change Initiative) product	R^2 = 0.38 and RMSE = 0.099 m^3/m^3
Sánchez-Ruiz et al., 2014	SMAP level-2 product	R^2 = 0.37, ubRMSE = 0.043 m^3/m^3 (descending overpass) R^2 = 0.52, ubRMSE = 0.04 m^3/m^3 (ascending overpass)
Colliander et al., 2017b	SMAP level-2 product	R^2 = 0.41, RMSD = 0.053 m^3/m^3 (1 km) R^2 = 0.54, RMSD = 0.037 m^3/m^3 (3 km)

Program (Program Manager Dr. Jared Entin, Grant #NNX12AP75G) and the Department of Engineering Systems and Environment at the University of Virginia for support of this work.

References

Bédard, F., Crump, S., Gaudreau, J., 2006. A comparison between Terra MODIS and NOAA AVHRR NDVI satellite image composites for the monitoring of natural grassland conditions in Alberta, Canada. Can. J. Remote Sens. 32 (1), 44–50.

Bell, J.E., Palecki, M.A., Baker, C.B., Collins, W.G., Lawrimore, J.H., Leeper, R.D., Diamond, H.J., 2013b. US Climate Reference Network soil moisture and temperature observations. J. Hydrometeorol. 14 (3), 977–988.

Bell, Jesse E., Palecki, Michael A., Bruce Baker, C., Collins, William G., Lawrimore, Jay H., Leeper, Ronald D., Hall, Mark E., et al., 2013a. US Climate Reference Network soil moisture and temperature observations. J. Hydrometeorol. 14 (3), 977–988.

Bindlish, R., Barros, A.P., 2002. Subpixel variability of remotely sensed soil moisture: an inter-comparison study of SAR and ESTAR. IEEE Trans. Geosci. Remote Sens. 40 (2), 326–337.

Bindlish, R., Cosh, M.H., Jackson, T.J., Koike, T., Fujii, H., Chan, S.K., et al., 2018. GCOM-W AMSR2 soil moisture product validation using core validation sites. IEEE J. Sel. Top. Appl. Earth Obs. Remote Sens. 11 (1), 209–219.

Bindlish, R., Jackson, T., Cosh, M., Zhao, T., O'neill, P. 2015. Global soil moisture from the Aquarius/SAC-D satellite: Description and initial assessment. IEEE Geoscience and Remote Sensing Letters, 12(5), 923-927.

Bogena, H.R., Huisman, J.A., Baatz, R., Hendricks Franssen, H.-J., Vereecken, H., 2013. Accuracy of the cosmic-ray soil water content probe in humid forest ecosystems: The worst case scenario. Water Resources Research 49(9), 5778-5791.

Bolten, J.D., Lakshmi, V., Njoku, E.G., 2003. Soil moisture retrieval using the passive/active L-and S-band radar/radiometer. IEEE Trans. Geosci. Remote Sens. 41 (12), 2792–2801.

Carlson, T., 2007. An overview of the" triangle method" for estimating surface evapotranspiration and soil moisture from satellite imagery. Sensors 7 (8), 1612–1629.

Chan, S.K., Bindlish, R., O'Neill, P.E., Njoku, E., Jackson, T., Colliander, A., et al., 2016. Assessment of the SMAP passive soil moisture product. IEEE Trans. Geosci. Remote Sens. 54 (8), 4994–5007.

Chan, S.K., Bindlish, R., O'Neill, P., Jackson, T., Njoku, E., Dunbar, S., et al., 2018. Development and assessment of the SMAP enhanced passive soil moisture product. Remote Sens. Environ. 204, 931–941.

Colliander, A., Fisher, J.B., Halverson, G., Merlin, O., Misra, S., Bindlish, R., et al., 2017b. Spatial downscaling of SMAP soil moisture using MODIS land surface temperature and NDVI during SMAPVEX15. IEEE Geosci. Remote Sens. Lett. 14 (11), 2107–2111.

Colliander, A., Jackson, T.J., Bindlish, R., Chan, S., Das, N., Kim, S.B., et al., 2017a. Validation of SMAP surface soil moisture products with core validation sites. Remote Sens. Environ. 191, 215–231.

Coopersmith, E.J., Cosh, M.H., Bell, J.E., Crow, W.T., 2016. Multi-profile analysis of soil moisture within the US Climate Reference Network. Vadose Zone J. 15 (1).

Cosh, M.H., Jackson, T.J., Bindlish, R., Prueger, J.H., 2004. Watershed scale temporal and spatial stability of soil moisture and its role in validating satellite estimates. Remote Sens. Environ. 92 (4), 427–435.
Dandridge, C., Fang, B., Lakshmi, V., 2020. Downscaling of SMAP Soil Moisture in the Lower Mekong River Basin. Water 12 (1), 56.
Diamond, H.J., Karl, T.R., Palecki, M.A., Baker, C.B., Bell, J.E., Leeper, R.D., et al., 2013. US Climate Reference Network after one decade of operations: status and assessment. Bull. Am. Meteorol. Soc. 94 (4), 485–498.
Dirmeyer, Paul A., Jiexia Wu, Holly E. Norton, Wouter A. Dorigo, Steven M. Quiring, Trenton W. Ford, Joseph A. Santanello Jr et al., 2016. Confronting weather and climate models with observational data from soil moisture networks over the United States. Journal of Hydrometeorology 17(4), 1049-1067.
Dorigo, W.A., Wagner, W., Hohensinn, R., Hahn, S., Paulik, C., Xaver, A., et al., 2011. The International Soil Moisture Network: a data hosting facility for global in situ soil moisture measurements. Hydrol. Earth Syst. Sci. 15 (5), 1675–1698.
Dorigo, W.A., Xaver, A., Vreugdenhil, M., Gruber, A., Hegyiova, A., Sanchis-Dufau, A.D., et al., 2013. Global automated quality control of in situ soil moisture data from the International Soil Moisture Network. Vadose Zone J. 12 (3).
Ek, M.B., Mitchell, K.E., Lin, Y., Rogers, E., Grunmann, P., Koren, V., et al., 2003. Implementation of Noah land surface model advances in the National Centers for Environmental Prediction operational mesoscale Eta model. J. Geophys. Res.: Atmos. 108 (D22).
Fang, L., Hain, C.R., Zhan, X., Anderson, M.C., 2016. An inter-comparison of soil moisture data products from satellite remote sensing and a land surface model. Int. J. Appl. Earth Obs. Geoinf. 48, 37–50.
Fang, B., Lakshmi, V., 2014b. Soil moisture at watershed scale: remote sensing techniques. J. Hydrol. 516, 258–272.
Fang, B., Lakshmi, V., 2014a. AMSR-E soil moisture disaggregation using MODIS and NLDAS data. Remote Sens. Terrestrial Water Cycle 206, 277.
Fang, B., Lakshmi, V., Bindlish, R., Jackson, T.J., Cosh, M., Basara, J., 2013. Passive microwave soil moisture downscaling using vegetation index and skin surface temperature. Vadose Zone J. 12 (3).
Fang, B., Lakshmi, V., Bindlish, R., Jackson, T., 2018a. Downscaling of SMAP soil moisture using land surface temperature and vegetation data. Vadose Zone J. 17 (1).
Fang, B., Lakshmi, V., Bindlish, R., Jackson, T., 2018b. AMSR2 soil moisture downscaling using temperature and vegetation data. Remote Sens. 10 (10), 1575.
Fang, B., Lakshmi, V., Jackson, T., Bindlish, R., Colliander, A., 2019. Passive/active microwave soil moisture change disaggregation using SMAPVEX12 Data. J. Hydrol. 574, 1085–1098.
Ford, Trent W., Quiring, Steven M., 2019. Comparison of contemporary in situ, model, and satellite remote sensing soil moisture with a focus on drought monitoring. Water Resour. Res. 55 (2), 1565–1582.
Gillies, R.R., Kustas, W.P., Humes, K.S., 1997. A verification of the'triangle'method for obtaining surface soil water content and energy fluxes from remote measurements of the Normalized Difference Vegetation Index (NDVI) and surface e. Int. J. Remote Sens. 18 (15), 3145–3166.
Gruber, A., Dorigo, W.A., Zwieback, S., Xaver, A., Wagner, W., 2013. Characterizing coarse-scale representativeness of in situ soil moisture measurements from the International Soil Moisture Network. Vadose Zone J. 12 (2).
Han, X., Jin, R., Li, X., Wang, S., 2014. Soil moisture estimation using cosmic-ray soil moisture sensing at heterogeneous farmland. IEEE Geosci. Remote Sens. Lett. 11 (9), 1659–1663.
Hong, S., Lakshmi, V., Small, E.E., Chen, F., Tewari, M., Manning, K.W., 2009. Effects of vegetation and soil moisture on the simulated land surface processes from the coupled WRF/Noah model. J. Geophys. Res.: Atmos. 114 (D18).
Hou, A.Y., Kakar, R.K., Neeck, S., Azarbarzin, A.A., Kummerow, C.D., Kojima, M., et al., 2014. The global precipitation measurement mission. Bull. Am. Meteorol. Soc. 95 (5), 701–722.
Huffman, G.J., Bolvin, D.T., Braithwaite, D., Hsu, K., Joyce, R., Xie, P., Yoo, S.H., 2015. NASA global precipitation measurement (GPM) integrated multi-satellite retrievals for GPM (IMERG). Algorithm Theoretical Basis Document, Version 4 30.
Imaoka, K., Kachi, M., Fujii, H., Murakami, H., Hori, M., Ono, A., et al., 2010. Global Change Observation Mission (GCOM) for monitoring carbon, water cycles, and climate change. Proc. IEEE 98 (5), 717–734.
Jackson, T.J., 1993. III. Measuring surface soil moisture using passive microwave remote sensing. Hydrol. Process. 7 (2), 139–152.
Jackson, T.J., Cosh, M.H., Bindlish, R., Starks, P.J., Bosch, D.D., Seyfried, M., et al., 2010. Validation of advanced microwave scanning radiometer soil moisture products. IEEE Trans. Geosci. Remote Sens. 48 (12), 4256–4272.
Jackson, T.J., Bindlish, R., Cosh, M.H., Zhao, T., Starks, P.J., Bosch, D.D., et al., 2012. Validation of Soil Moisture and Ocean Salinity (SMOS) soil moisture over watershed networks in the US. IEEE Trans. Geosci. Remote Sens. 50 (5), 1530–1543.
Jakobi, J., Huisman, J.A., Vereecken, H., Diekkrüger, B., Bogena, H.R., 2018. Cosmic ray neutron sensing for simultaneous soil water content and biomass quantification in drought conditions. Water Resour. Res. 54 (10), 7383–7402.
Kerr, Y.H., Waldteufel, P., Wigneron, J.P., Martinuzzi, J.A.M.J., Font, J., Berger, M., 2001. Soil moisture retrieval from space: the Soil Moisture and Ocean Salinity (SMOS) mission. IEEE Trans. Geosci. Remote Sens. 39 (8), 1729–1735.
Kim, S., Balakrishnan, K., Liu, Y., Johnson, F., Sharma, A., 2017. Spatial disaggregation of coarse soil moisture data by using high-resolution remotely sensed vegetation products. IEEE Geosci. Remote Sens. Lett. 14 (9), 1604–1608.
Kim, H., Lakshmi, V., 2018. Use of Cyclone Global Navigation Satellite System (CYGNSS) observations for estimation of soil moisture. Geophys. Res. Lett. 45 (16), 8272–8282.
Kim, H., Parinussa, R., Konings, A.G., Wagner, W., Cosh, M.H., Lakshmi, V., et al., 2018. Global-scale assessment and combination of SMAP with ASCAT (active) and AMSR2 (passive) soil moisture products. Remote Sens. Environ. 204, 260–275.
Lakshmi, V., 2004. The role of satellite remote sensing in the prediction of ungauged basins. Hydrol. Process. 18 (5), 1029–1034.
Lakshmi, V., Susskind, J., 2000. Comparison of TOVS-derived land surface variables with ground observations. J. Geophys. Res.: Atmos. 105 (D2), 2179–2190.
Lakshmi, V., Wood, E.F., Choudhury, B.J., 1997. A soil-canopy-atmosphere model for use in satellite microwave remote sensing. J. Geophys. Res.: Atmos. 102 (D6), 6911–6927.
Lakshmi, V., Czajkowski, K., Dubayah, R., Susskind, J., 2001. Land surface air temperature mapping using TOVS and AVHRR. Int. J. Remote Sens. 22 (4), 643–662.
Lakshmi, V., Hong, S., Small, E.E., Chen, F., 2011. The influence of the land surface on hydrometeorology and ecology: new advances from modeling and satellite remote sensing. Hydrol. Res. 42 (2–3), 95–112.
Lakshmi, V., 2013. Remote sensing of soil moisture. ISRN Soil Science, 2013.
Lakshmi, V. (Ed.), 2014. Remote Sensing of the terrestrial water cycle (Vol. 206). John Wiley & Sons.
Le Vine, D.M., Griffis, Andrew J., Swift, Calvin T., Jackson, Thomas J., 1994. ESTAR: a synthetic aperture microwave radiometer for remote sensing applications. Proc. IEEE 82 (12), 1787–1801.
Mallick, K., Bhattacharya, B.K., Patel, N.K., 2009. Estimating volumetric surface moisture content for cropped soils using a soil wetness index based on surface temperature and NDVI. Agric. For. Meteorol. 149 (8), 1327–1342.
Matsushima, D., Kimura, R., Shinoda, M., 2012. Soil moisture estimation using thermal inertia: potential and sensitivity to data conditions. J. Hydrometeorol. 13 (2), 638–648.
McNairn, H., Jackson, T.J., Wiseman, G., Belair, S., Berg, A., Bullock, P., et al., 2014. The soil moisture active passive validation experiment 2012 (SMAPVEX12): prelaunch calibration and validation of the SMAP soil moisture algorithms. IEEE Trans. Geosci. Remote Sens. 53 (5), 2784–2801.
Merlin, O., Al Bitar, A., Walker, J.P., Kerr, Y., 2010. An improved algorithm for disaggregating microwave-derived soil moisture based on red, near-infrared and thermal-infrared data. Remote Sens. Environ. 114 (10), 2305–2316.
Merlin, Olivier, Escorihuela, Maria José, Mayoral, Miquel Aran, Hagolle, Olivier, Bitar, Ahmad Al, Kerr, Yann, 2013. Self-calibrated evaporation-based disaggregation of SMOS soil moisture: an evaluation study at 3 km and 100 m resolution in Catalunya, Spain. Remote Sens. Environ. 130, 25–38.
Merlin, O., Malbéteau, Y., Notfi, Y., Bacon, S., Khabba, S., Jarlan, L., 2015. Performance metrics for soil moisture downscaling methods: application to DISPATCH data in central Morocco. Remote Sens. 7 (4), 3783–3807.
Minacapilli, M., Iovino, M., Blanda, F., 2009. High resolution remote estimation of soil surface water content by a thermal inertia approach. J. Hydrol. 379 (3–4), 229–238.
Mishra, V., Ellenburg, W.L., Griffin, R.E., Mecikalski, J.R., Cruise, J.F., Hain, C.R., Anderson, M.C., 2018. An initial assessment of a SMAP soil moisture disaggregation scheme using TIR surface evaporation data over the continental United States. Int. J. Appl. Earth Obs. Geoinf. 68, 92–104.
Mitchell, K.E., Lohmann, D., Houser, P.R., Wood, E.F., Schaake, J.C., Robock, A., et al., 2004. The multi-institution North American Land Data Assimilation System (NLDAS): utilizing multiple GCIP products and partners in a continental distributed hydrological modeling system. J. Geophys. Res.: Atmos. 109 (D7).
Moghaddam, M., Entekhabi, D., Goykhman, Y., Li, K., Liu, M., Mahajan, A., Nayyar, A., Shuman, D., Teneketzis, D., 2010. A wireless soil moisture smart sensor web using physics-based optimal control: concept and initial demonstrations. IEEE J. Sel. Top. Appl. Earth Obs. Remote Sens. 3 (4), 522–535.
Narayan, U., Lakshmi, V., 2008. Characterizing subpixel variability of low resolution radiometer derived soil moisture using high resolution radar data. Water Resour. Res. 44 (6).
Narayan, U., Lakshmi, V., Njoku, E.G., 2004. Retrieval of soil moisture from passive and active L/S band sensor (PALS) observations during the Soil Moisture Experiment in 2002 (SMEX02). Remote Sens. Environ. 92 (4), 483–496.
Narayan, U., Lakshmi, V., Jackson, T.J., 2006. High-resolution change estimation of soil moisture using L-band radiometer and radar observations made during the SMEX02 experiments. IEEE Trans. Geosci. Remote Sens. 44 (6), 1545–1554.
Njoku, E.G., Entekhabi, D., 1996. Passive microwave remote sensing of soil moisture. J. Hydrol. 184 (1–2), 101–129.
Njoku, E.G., Jackson, T.J., Lakshmi, V., Chan, T.K., Nghiem, S.V., 2003. Soil moisture retrieval from AMSR-E. IEEE Trans. Geosci. Remote Sens. 41 (2), 215–229.
Oki, T., Imaoka, K., Kachi, M., 2010. AMSR instruments on GCOM-W1/2: Concepts and applications. In Geoscience and remote sensing symposium (IGARSS), 2010 IEEE International (pp. 1363-1366). IEEE.
Pedelty, J., Devadiga, S., Masuoka, E., Brown, M., Pinzon, J., Tucker, C., et al., 2007. Generating a long-term land data record from the AVHRR and MODIS instruments. In Geoscience and Remote Sensing Symposium, 2007. IGARSS 2007. IEEE International (pp. 1021-1025). IEEE.
Peng, J., Niesel, J., Loew, A., 2015. Evaluation of soil moisture downscaling using a simple thermal-based proxy–the REMEDHUS network (Spain) example. Hydrol. Earth Syst. Sci. 19 (12), 4765–4782.
Peng, J., Loew, A., Zhang, S., Wang, J., Niesel, J., 2016. Spatial downscaling of satellite soil moisture data using a vegetation temperature condition index. IEEE Trans. Geosci. Remote Sens. 54 (1), 558–566.
Peng, J., Loew, A., Merlin, O., Verhoest, N.E., 2017. A review of spatial downscaling of satellite remotely sensed soil moisture. Rev. Geophys. 55 (2), 341–366.
Piepmeier, J.R., Johnson, J.T., Mohammed, P.N., Bradley, D., Ruf, C., Aksoy, M., et al., 2013. Radio-frequency interference mitigation for the soil moisture active passive microwave radiometer. IEEE Trans. Geosci. Remote Sens. 52 (1), 761–775.
Piles, M., Camps, A., Vall-Llossera, M., Corbella, I., Panciera, R., Rudiger, C., et al., 2011. Downscaling SMOS-derived soil moisture using MODIS visible/infrared data. IEEE Trans. Geosci. Remote Sens. 49 (9), 3156–3166.

Piles, María, Sánchez, Nilda, Vall-llossera, Mercè, Camps, Adriano, Martínez-Fernández, José, Martínez, Justino, González-Gambau, Verónica, 2014. A downscaling approach for SMOS land observations: evaluation of high-resolution soil moisture maps over the Iberian Peninsula. IEEE J. Sel. Top. Appl. Earth Obs. Remote Sens. 7 (9), 3845–3857.

Rosolem, R., Shuttleworth, W.J., Zreda, M., Franz, T.E., Zeng, X., Kurc, S.A., 2013. The effect of atmospheric water vapor on neutron count in the cosmic-ray soil moisture observing system. J. Hydrometeorol. 14 (5), 1659–1671.

Sabaghy, S., Walker, J.P., Renzullo, L.J., Jackson, T.J., 2018. Spatially enhanced passive microwave derived soil moisture: capabilities and opportunities. Remote Sens. Environ. 209, 551–580.

Sánchez-Ruiz, Sergio, Piles, María, Sánchez, Nilda, Martínez-Fernández, José, Vall-llossera, Mercè, Camps, Adriano, 2014. Combining SMOS with visible and near/shortwave/thermal infrared satellite data for high resolution soil moisture estimates. J. Hydrol. 516, 273–283.

Schaake, J.C., Duan, Q., Koren, V., Mitchell, K.E., Houser, P.R., Wood, E.F., et al., 2004. An intercomparison of soil moisture fields in the North American Land Data Assimilation System (NLDAS). J. Geophys. Res.: Atmos. 109 (D1).

Schaefer, Garry L., Cosh, Michael H., Jackson, Thomas J., 2007. The USDA natural resources conservation service soil climate analysis network (SCAN). J. Atmos. Oceanic Technol. 24 (12), 2073–2077.

Schmugge, T., Jackson, T.J., 1994. Mapping surface soil moisture with microwave radiometers. Meteorol. Atmos. Phys. 54 (1–4), 213–223.

Schmugge, T., O'Neill, P.E., Wang, J.R., 1986. Passive microwave soil moisture research. IEEE Trans. Geosci. Remote Sens. 1, 12–22.

Senanayake, I.P., Yeo, I.Y., Tangdamrongsub, N., Willgoose, G.R., Hancock, G.R., Wells, T., Fang, B., Lakshmi, V., Walker, J.P., 2019. An in-situ data based model to downscale radiometric satellite soil moisture products in the Upper Hunter Region of NSW, Australia. J. Hydrol. 572, 820–838.

Spencer, Michael W., Chen, Curtis W., Ghaemi, Hirad, Chan, Samuel F., Belz, John E., 2013. RFI characterization and mitigation for the SMAP radar. IEEE Trans. Geosci. Remote Sens. 51 (10), 4973–4982.

Sridhar, V., Jaksa, W.T.A., Fang, B., Lakshmi, V., Hubbard, K.G., Jin, X., 2013. Evaluating bias-corrected AMSR-E soil moisture using in situ observations and model estimates. Vadose Zone J. 12 (3).

Tagesson, T., Horion, S., Nieto, H., Fornies, V.Z., González, G.M., Bulgin, C.E., et al., 2018. Disaggregation of SMOS soil moisture over West Africa using the Temperature and Vegetation Dryness Index based on SEVIRI land surface parameters. Remote Sens. Environ. 206, 424–441.

Tucker, C.J., 1979. Red and photographic infrared linear combinations for monitoring vegetation. Remote Sens. Environ. 8 (2), 127–150.

Wagner, W., Hahn, S., Kidd, R., Melzer, T., Bartalis, Z., Hasenauer, S., et al., 2013. The ASCAT soil moisture product: a review of its specifications, validation results, and emerging applications. Meteorol. Z. 22 (1), 5–33.

Wan, Z., Li, Z.L., 1997. A physics-based algorithm for retrieving land-surface emissivity and temperature from EOS/MODIS data. IEEE Trans. Geosci. Remote Sens. 35 (4), 980–996.

Willmott, Cort J., 1982. Some comments on the evaluation of model performance. Bull. Am. Meteorol. Soc. 63 (11), 1309–1313.

Xia, Y., Ek, M., Sheffield, J., Livneh, B., Huang, M., Wei, H., et al., 2013. Validation of Noah-simulated soil temperature in the North American land data assimilation system phase 2. J. Appl. Meteorol. Climatol. 52 (2), 455–471.

Zhan, X., Fang, L., Liu, J., Hain, C., Yin, J., Schull, M., et al., 2017. Fusing microwave and optical satellite observations for high resolution soil moisture data products. In Geoscience and Remote Sensing Symposium (IGARSS), 2017 IEEE International (pp. 2519-2522). IEEE.

Zhao, W., Li, A., 2013. A downscaling method for improving the spatial resolution of AMSR-E derived soil moisture product based on MSG-SEVIRI data. Remote Sens. 5 (12), 6790–6811.

Zhao, W., Sánchez, N., Lu, H., Li, A., 2018. A spatial downscaling approach for the SMAP passive surface soil moisture product using random forest regression. J. Hydrol. 563, 1009–1024.

Zreda, M., Shuttleworth, W.J., Zeng, X., Zweck, C., Desilets, D., Franz, T., Rosolem, R., 2012. COSMOS: the cosmic-ray soil moisture observing system. Hydrol. Earth Syst. Sci. 16 (11), 4079–4099.